# A novel approach to characterize the variability in mass-Dimension relationships: results from MC3E

Joseph A. Finlon[1], Greg M. McFarquhar[2,3], Stephen W. Nesbitt[1], Robert M. Rauber[1], Hugh Morrison[4], Wei Wu[2], and Pengfei Zhang[2,5]

[1]Department of Atmospheric Sciences, University of Illinois at Urbana-Champaign, Urbana, IL 61801, United States
[2]Cooperative Institute for Mesoscale Meteorological Studies, University of Oklahoma, Norman, OK 73072, United States
[3]School of Meteorology, University of Oklahoma, Norman, OK 73072, United States
[4]National Center for Atmospheric Research, Boulder, CO 80301, United States
[5]NOAA/National Severe Storms Laboratory, Norman, OK 73072, United States

**Correspondence:** Greg M. McFarquhar (mcfarq@ou.edu)

**Abstract.** Mass-dimension ($m$-$D$) relationships determining bulk microphysical properties such as total water content ($TWC$) and radar reflectivity factor ($Z$) from particle size distributions are used in both numerical models and remote sensing retrievals. The $a$ and $b$ coefficients representing $m = aD^b$ relationships, however, can vary significantly depending on meteorological conditions, particle habits, definition of particle maximum dimension, the probes used to obtain the data, techniques used to
5   process the cloud probe data, and other unknown reasons. Thus, considering a range of $a,b$ coefficients may be more applicable for use in numerical models and remote sensing retrievals. Microphysical data collected by two-dimensional optical array probes (OAPs) installed on the University of North Dakota Citation aircraft during the Mid-latitude Continental Convective Clouds Experiment (MC3E) were used in conjunction with $TWC$ data from a Nevzorov probe and ground-based S-band radar data to determine $a$ and $b$ using a technique that minimizes the chi-square difference between $TWC$ and $Z$ derived from the
10  OAPs and that directly measured by a $TWC$ probe and radar. All $a$ and $b$ within a specified tolerance were regarded as equally plausible solutions. Of the 16 near-constant temperature flight legs analyzed during the 25 April, 20 May, and 23 May 2011 events, the derived surfaces of solutions on the first two days where the aircraft sampled stratiform cloud had a larger range in $a$ and $b$ for lower temperature environments that corresponded to less variability in $N(D)$, $TWC$, and $Z$ for a flight leg. Because different regions of the storm were sampled on 23 May, differences in the variability of $N(D)$, $TWC$, and $Z$ influenced the
15  distribution of chi-square values in $(a,b)$ phase space and the specified tolerance in a way that yielded 6.7 times fewer plausible solutions compared to the flight legs on the other dates. These findings show the importance of representing the variability in $a,b$ coefficients for numerical modeling and remote sensing studies rather than assuming fixed values, as well as the need to further explore how these surfaces depend on environmental conditions in ice and mixed phase clouds.

## 1   Introduction

20  Mass-dimension ($m$-$D$) relations are required to link bulk microphysical properties, such as total water content ($TWC$) and forward model radar reflectivity factor ($Z$), to ice crystal particle size distributions (PSDs). These relations are extensively

assumed in both numerical models and remote sensing retrievals and relate a particle's mass ($m$) to its size, typically defined by its maximum dimension projected onto a 2-D plane ($D$), by means of a power law in the form $m = aD^b$. Past studies have suggested the exponent $b$ is related to the exponent in surface area-dimension relationships (Fontaine et al., 2014) or to a particle's fractal dimension (Schmitt and Heymsfield, 2010). The prefactor $a$ has some dependence on $b$ and on the particle

5    density.

Prior $m$-$D$ relationships have been determined using cloud probe data obtained in a variety of environmental conditions. Figure 1a shows how $m$-$D$ coefficients derived from previous studies vary depending on the types of clouds sampled. Coefficients derived using data over mountainous terrain (e.g., Nakaya and Terada, 1935; Locatelli and Hobbs, 1974), cirrus clouds (e.g., Heymsfield, 1972; Hogan et al., 2000), convective clouds (e.g., Liu and Curry, 2000; Cazenave et al., 2016; Leroy et al., 2016),

10   regions of large scale ascent (e.g., Szyrmer and Zawadzki, 2010), and computer-generated shapes (e.g., Matrosov, 2007; Olson et al., 2016) are shown. A total of 119 relations are shown in Fig. 1. The range of $a$ in Fig. 1a spans five orders of magnitude, with variations in $a$ spanning 3 orders of magnitude or more even for measurements obtained in the same cloud type. The exponent $b$ ranges between one and three within the same environments. The relations in Fig. 1 were derived using data collected by different types and versions of cloud probes, using different algorithms to process the data. McFarquhar et al. (2017) have

15   shown that it can be difficult to disentangle the dependence of derived microphysical parameters on environmental conditions from the dependence on the probes used to collect and the methods to process the data.

Figure 1b shows that $m$-$D$ coefficients also vary depending on the technique used to derive the $m$-$D$ relations. In some studies the maximum dimension of frozen hydrometeors was recorded before the crystal was melted and the single particle mass subsequently measured (Magono and Nakamura, 1965; Zikmunda and Vali, 1972; Mitchell et al., 1990), whereas other

20   studies used measurements of either bulk mass measured by an evaporation probe (Heymsfield et al., 2002; Cotton et al., 2013; Xu and Mace, 2017) or bulk Z observed by a collocated radar measurement (McFarquhar et al., 2007b; Maahn et al., 2015) in combination with in situ measured PSDs. Further, Wu and McFarquhar (2016) showed inconsistencies in how D is defined (Mitchell and Arnott, 1994; Brown and Francis, 1995; McFarquhar and Heymsfield, 1996; Heymsfield et al., 2013; Lawson et al., 2015; Korolev and Field, 2015) can also impact $m$-$D$ relations. For example, they noted ice water content ($IWC$) values

25   derived using various definitions of $D$ ranged between 60 and 160% of the $IWC$ derived using a smallest enclosing circle to define $D$.

Remote sensing retrieval schemes and model microphysical parameterization schemes are sensitive to the choice of $m$-$D$ relationship. For example, Delanoë and Hogan (2010) showed that differences in the mean extinction, $IWC$, and effective radius retrieved from spaceborne remote sensors were 28, 9, and 30%, respectively, depending on whether $m$-$D$ relations of

30   spherical aggregates (Brown and Francis, 1995, hereafter BF95) or bullet rosettes (Mitchell, 1996) were used. McCumber et al. (1991) showed time series of modeled precipitation rate with differences of 20 to 50% depending on assumptions about particle density, which are affected by the $m$-$D$ relation. Later studies (e.g., Mitchell, 1996; Erfani and Mitchell, 2016) attributed differences in model output to the influence of particle mass on terminal fall velocities.

Although many studies have established $m$-$D$ relations for specific cases, a universal $m$-$D$ relationship has not been found

35   nor can a single relation be expected to represent the wide range of crystal habits and sizes within clouds occurring at different

temperatures, locations, or formed by different mechanisms. Moreover, a single relationship cannot account for the natural variability of cloud properties such as particle size, shape, and density that occurs even in similar environmental conditions. Thus, some alternate approach is more appropriate for modeling and remote sensing studies that considers multiple *m-D* relations over many retrievals or model simulations to evaluate the variability in the ensemble results.

5  While previous studies (e.g., McFarquhar et al., 2007b; Heymsfield et al., 2010; Mascio et al., 2017) have considered how *m-D* relations vary with environmental conditions, such as temperature, the derived relations were fixed regardless of potential fluctuations for that environment. Further uncertainties were associated with measurement errors induced by shattering of large ice crystals on probe tips and subsequent detection within the probe's sample volume (Field et al., 2003), the processing techniques used (McFarquhar et al., 2017), and from the statistical counting of particles (e.g., Hallett, 2003; McFarquhar et al.,

10  2007a). The approach by Fontaine et al. (2014) evaluated the variability in the prefactor *a* for an assumed exponent *b* for two field projects, but ultimately still derived a single *m-D* relationship for each dataset based on the mean conditions.

Extending the approach of McFarquhar et al. (2015), which derived a volume of equally realizable solutions within the phase space of the three gamma fit parameters (concentration $N_0$, shape $\mu$, and slope $\lambda$) characterizing PSDs, a novel approach is used here to determine equally valid *m-D* relations for a given environment. Data from a variety of environments sampled during

15  the Mid-latitude Continental Convective Clouds Experiment (MC3E) are used to establish a surface of equally plausible *a* and *b* coefficients in (*a,b*) phase space using a technique that minimizes the chi-square difference between the *TWC* and *Z* derived from the PSDs measured by optical array probes (OAPs) and that directly measured by a *TWC* probe and radar.

The remainder of this paper is organized as follows. Section 2 outlines the datasets used and the methodology to process the radar and microphysics data, while Sect. 3 describes the technique employed to determine the surfaces of *m-D* coefficients. A

20  brief description of the MC3E cases used in this study is provided in Sect. 4, and the surfaces of coefficients are derived and discussed in Sect. 5. A summary of the technique and its implications for numerical modeling and remote sensing retrieval schemes are given in Sect. 6.

## 2  Data and methodology

The data in this study were collected within mesoscale convective systems (MCSs) during the 2011 Mid-latitude Continental

25  Convective Clouds Experiment (MC3E; Jensen et al., 2016). The study presented here uses data from cloud microphysical instruments aboard the University of North Dakota (UND) Cessna Citation II aircraft and from the Vance Air Force Base, OK (KVNX) Weather Surveillance Radar-1988 Doppler (WSR-88D) radar.

### 2.1  Identification of coincident aircraft/radar data

The use of airborne microphysical measurements and radar data collected from the ground allowed sampling of the same region

30  of the cloud from microphysical and remote sensing perspectives. Use of the Airborne Weather Observation Toolkit (https://github.com/swnesbitt/AWOT) radar matching algorithm and the Python ARM Radar Toolkit (Py-ART; Helmus and Collis, 2016) permitted calculation of radar *Z* in the vicinity of the aircraft for each second of in situ cloud distributions measured

during flight. The algorithm organizes all radar gates in a 3-Dimensional space (Maneewongvatana and Mount, 1999) for efficient acquisition of radar parameters at nearby radar range gates. The Barnes (1964) interpolation technique is then applied to data at the eight nearest gates within 500 m of the aircraft's location, ignoring vertically adjacent gates beyond a range of 65 km as the beamwidth exceeds the 500 m threshold, to obtain an averaged $Z$ at the aircraft location.

5   To compare microphysical properties with radar-measured Z for constant altitude flight legs at similar environmental temperature, only those times when the radar and microphysical datasets are coincident and the temperature varies by less than 1 °C were considered. To reduce uncertainty due to counting statistics in the measured PSDs, microphysical data were averaged over a 10 s period. The *TWC* measurements and matched radar $Z$ were then averaged over the same 10 s period, with each 10 s interval assigned as a coincident point. Table 1 lists the start and end times, mean altitude, and temperature for each of the 16

10   constant-temperature flight legs flown when the UND Citation was in cloud. Observations where the mean *TWC* for each 10 s interval $< 0.05$ g m$^{-3}$ were ignored as the values were considered either below the noise threshold of the Nevzorov probe or optically thin cloud. To further constrain the study to periods when clouds were dominated by ice phase hydrometeors such that $TWC \approx IWC$ and to reduce the impact of liquid phase hydrometeors on the derived *TWC* and *Z*, observations were excluded from the analysis if the 10 s mean concentration from the cloud droplet probe exceeded 10 cm$^{-3}$ which usually corresponds

15   to the presence of water (Heymsfield et al., 2011). Of the coincident observations considered, 12.3% were excluded from the analysis based on these criteria. A total of 493 coincident observations were retained for this analysis.

## 2.2   Radar measurements

Data from the KVNX S-band (10 cm wavelength) radar were used in this study. Although the NASA dual-polarization (N-Pol) S-band Doppler radar was deployed during MC3E, mechanical issues prevented reliable collection of data for two of the three

20   events examined here. Radars at other wavelengths collected data during MC3E. However, attenuation through liquid portions of the cloud (e.g., Bringi et al., 1990; Park et al., 2005; Matrosov, 2008) and non-Rayleigh scattering by larger particles (e.g., Lemke and Quante, 1999; Matrosov, 2007) could not be accounted for, and prompted exclusive use of the S-band radar.

Radar reflectivity factor values for gates near the UND Citation (Sect. 2.1) were used to obtain the average value of $Z$ using the radar matching algorithm only if the following criteria were met: correlation coefficient $\rho_{HV} \geq 0.75$, sigma differential

25   phase $SDP \leq 12$ deg$^2$ km$^{-2}$, differential reflectivity $-2 \leq Z_{DR} \leq 3$ dB, and reflectivity texture (defined as the standard deviation in $Z$ of the nearest 5 gates) $< 7$ dBZ. These ranges represent acceptable values for echoes based on previous studies (Bringi and Chandrasekar, 2001). Radar gates not meeting these criteria were masked, reducing the likelihood of including gates with excessive signal noise due to clutter or weak signal, contamination by the aircraft, or other factors. For instances where the matched $Z$ changed by more than 2 dBZ for subsequent 1 s points (fewer than one percent of the observations), all

30   radar gates factored into the radar matching algorithm were inspected by eye to ensure that no outlier values were responsible for the jump in the matched $Z$. Of the observations that were manually inspected, all appeared spatially consistent with no outliers present, and as such remained in the averaging routine of the matching algorithm discussed in Sect. 2.1.

### 2.3 Microphysical measurements

During MC3E the Citation aircraft sampled clouds in situ, with most data collected in ice phase clouds between the melting layer and cloud top (Jensen et al., 2016). A suite of microphysical instruments was installed on the aircraft, including OAPs, which were used to image particles and derive PSDs, and a TWC probe. Specifics on the instrumentation and steps used to

5    process the data are described below.

#### 2.3.1 OAP data

A cloud imaging probe (CIP), a 2D cloud (2D-C) probe, and a High Volume Precipitation Spectrometer Version 3 (HVPS-3) sized particles by shadowing photodiode arrays attached to fast response electronics. Data from the 2D-C and HVPS-3 were combined to create a composite PSD, permitting particles between 150 μm and 19.2 mm to be considered in the analysis.

10   Following Wu and McFarquhar (2016), the number distribution function $N(D)$ was obtained using the 2D-C for particles with $D < 1$ mm and the HVPS-3 for $D > 1$ mm. The 1 mm cutoff was chosen since $N(D)$ between the two OAPs agreed on average within 5 percent for $0.8 \leq D \leq 1.2$ mm. Given uncertainties in the probe's sample area and limitations of its depth of field for smaller particle sizes (Baumgardner and Korolev, 1997), particles with $D < 150$ μm were not included in the analysis.

The OAP data were processed using the University of Illinois/Oklahoma OAP Processing Software (UIOOPS; McFarquhar

15   et al., 2018). Numerous morphological properties were calculated (e.g., particle maximum dimension, projected area, perimeter, area ratio, and habit) for individual particles, and PSDs were determined for each second of flight. Following Heymsfield and Baumgardner (1985) and Field (1999), only particles with a center of mass within the OAP's field of view were considered as otherwise there is too much uncertainty in particle shape. Shattered artifacts were removed using a threshold for the required time between particles entering the sample volume (inter-arrival time; Field et al., 2006). The inter-arrival times typically

20   follow a bimodal distribution, with naturally-occurring particles having a mode with longer inter-arrival times and shattered artifacts having shorter inter-arrival times (e.g., Field et al., 2003). A constant inter-arrival time threshold of $10^{-5}$ s was applied to the 2D-C data, with particles below this threshold identified as artifacts.

#### 2.3.2 TWC data

The TWC was determined from the Nevzorov probe using the power required to melt or evaporate ice particles impinging on

25   the inside of a cone (e.g., Nevzorov, 1980; Korolev et al., 1998). The probe used had a deeper cone than previous designs with a $60°$ vertex angle (as opposed to a $120°$ angle) that prevented many particles from bouncing out of the cone. Because previous studies suggested that particles with $D > 4$ mm can bounce out of even the deeper cone (Wang et al., 2015), $TWC$ may be underestimated when such particles are present. However, Korolev et al. (2013) showed that the ratio of the Nevzorov $IWC$ to that derived from the measured PSDs using the BF95 relation did not significantly vary with particle maximum dimension.

30   Of the coincident points belonging to constant altitude flight legs in this study, 79.2% of the observations had cumulative mass estimates using the BF95 relation from particles with $D \leq 4$ mm contributing at least 80% to the total mass. Therefore, measurements of $TWC$ were included irrespective of whether $D_{\mathrm{max}} > 4$ mm.

## 3 Development of equally plausible (*a*,*b*) surfaces

In this section, a method for determining a surface of equally realizable solutions for *m-D* coefficients in the phase space of (*a*,*b*) coefficients is described. The surface of these coefficients is determined through a procedure that minimizes the $\chi^2$ differences between the *TWC* and *Z* derived from *N(D)* and that directly measured by the Nevzorov and ground-based radar, respectively. The minimization procedure is carried out for each constant-temperature flight leg (defined by temperature varying by less than 1 °C) for the MC3E cases studied. This approach follows that of McFarquhar et al. (2015) who developed volumes of equally realizable $N_0$, $\mu$, and $\lambda$ characterizing observed *N(D)* as gamma distributions for observations obtained during the Indirect and Semi-Direct Aerosol Campaign (ISDAC) and the NASA African Monsoon Multidisciplinary Analyses project (NAMMA).

For an individual 10 s sample, the metric defining the difference between the *TWC* and *Z* derived from *N(D)* for a specific *a* and *b* and that directly measured by the Nevzorov and ground-based radar, respectively, is given by $TWC_{\mathrm{diff}}$ and $Z_{\mathrm{diff}}$ as follows:

$$TWC_{\mathrm{diff}} = \left[ \frac{TWC - TWC_{\mathrm{SD}}(a,b)}{\sqrt{TWC \times TWC_{\mathrm{SD}}(a,b)}} \right]^2 \text{ and} \tag{1}$$

$$Z_{\mathrm{diff}} = \left[ \frac{\sqrt{Z} - \sqrt{Z_{\mathrm{SD}}(a,b)}}{\sqrt{\sqrt{Z} \times \sqrt{Z_{\mathrm{SD}}(a,b)}}} \right]^2. \tag{2}$$

In this study, $TWC_{\mathrm{diff}}$ and $Z_{\mathrm{diff}}$ are computed for all points in the domain of values encompassing $5 \times 10^{-4} < a < 0.35$ g cm$^{-b}$ and $0.20 < b < 5.00$ at increments of $5 \times 10^{-4}$ g cm$^{-b}$ and 0.01, respectively. The $TWC_{\mathrm{SD}}(a,b)$ and $Z_{\mathrm{SD}}(a,b)$ derived from the PSD rely on the mass of individual particles determined for each *a* and *b* following the method of Hogan et al. (2006), and account for the different dielectric constants for water ($|K_w|^2 = 0.93$) and ice ($|K_{ice}|^2 = 0.17$). An example of $TWC_{\mathrm{diff}}$ and $Z_{\mathrm{diff}}$ values computed in (*a*,*b*) phase space for a 10 s averaged PSD beginning at 13:56:45 UTC on 20 May 2011 is shown in Fig. 2a. The color representing $TWC_{\mathrm{diff}} + Z_{\mathrm{diff}}$ is shaded on a logarithmic scale to more easily show the range of values. The smallest swath of values, arbitrarily chosen as being $TWC_{\mathrm{diff}} + Z_{\mathrm{diff}} \leq 1$ within the region outlined black, spans *b* values of 1.13 to 4.72. The curvature in the outlined region highlights the correlation of *a* and *b* so that similar *m* can be obtained from very different *b* by adjusting *a* accordingly. Considering both $TWC_{\mathrm{diff}}$ and $Z_{\mathrm{diff}}$ allows the shape and placement of the smallest swath of values to adjust according to two different moments of the PSD since conditions impact *TWC* differently than *Z*. Using two constraints on the $\chi^2$ minimization technique therefore provides additional insight into the microphysical properties as discussed in Sect. 5.

The chi-square statistic for a flight leg, defined as

$$\chi^2(a,b) = \frac{1}{N} \sum_{i=1}^{N} TWC_{\mathrm{diff}}(i) + Z_{\mathrm{diff}}(i), \tag{3}$$

involves a summation over all N 10 s coincident observations represented by the index *i* and normalized by N. When $\chi^2$ is computed by summing over all N points in the flight leg, the region with the smallest $\chi^2$ ($\chi^2 \leq 1$; outlined region in Fig. 2b) is

smaller than the region in Fig. 2a because different $(a,b)$ minimize $\chi^2$ for each of the individual PSDs in the 5 minute period depicted. Therefore, overall the $\chi^2$ values are higher than the $TWC_{\text{diff}} + Z_{\text{diff}}$ computed for each $(a,b)$. The point in Fig. 2b shows the $a$ and $b$ that minimizes $\chi^2$, hereafter represented as $\chi^2_{\min}$, which represents the most likely $a$ and $b$ values.

To represent the uncertainty in the derived coefficients for each flight leg, all $a$ and $b$ fulfilling $\chi^2 \leq \chi^2_{\min} + \Delta\chi^2$ are assumed to be equally plausible solutions. McFarquhar et al. (2015) defined the confidence region $\Delta\chi^2 = \max(\Delta\chi^2_1, \chi^2_{\min})$, where $\Delta\chi^2_1$ represented uncertainties in the PSD due to statistical sampling uncertainties and $\chi^2_{\min}$ characterized the robustness of the minimization procedure. Similar to their study, $\Delta\chi^2_1$ is determined here as

$$
\Delta\chi^2_1 = \frac{1}{N} \sum_{i=1}^{N} \begin{aligned} &\frac{1}{2}\left\{\left[\frac{TWC_{\text{SD,min}(i)} - TWC_{\text{SD}(i)}}{\sqrt{TWC_{\text{SD,min}(i)} \times TWC_{\text{SD}(i)}}}\right]^2 + \left[\frac{TWC_{\text{SD,max}(i)} - TWC_{\text{SD}(i)}}{\sqrt{TWC_{\text{SD,max}(i)} \times TWC_{\text{SD}(i)}}}\right]^2\right\} + \\ &\frac{1}{2}\left\{\left[\frac{\sqrt{Z_{\text{SD,min}(i)}} - \sqrt{Z_{\text{SD}(i)}}}{\sqrt{\sqrt{Z_{\text{SD,min}(i)}} \times \sqrt{Z_{\text{SD}(i)}}}}\right]^2 + \left[\frac{\sqrt{Z_{\text{SD,max}(i)}} - \sqrt{Z_{\text{SD}(i)}}}{\sqrt{\sqrt{Z_{\text{SD,max}(i)}} \times \sqrt{Z_{\text{SD}(i)}}}}\right]^2\right\}. \end{aligned} \tag{4}
$$

The different terms in Eq. (4) represent the difference in the minimum and maximum $TWC$ or $Z$ derived from the minimum and maximum $N(D)$ using the $(a,b)$ minimizing $\chi^2$ ($TWC_{\text{SD,min}}$ and $TWC_{\text{SD,max}}$ or $Z_{\text{SD,min}}$ and $Z_{\text{SD,max}}$) and that derived from the most likely $N(D)$ ($TWC_{\text{SD}}$ or $Z_{\text{SD}}$). Following McFarquhar et al. (2015), the minimum and maximum $N(D)$ are determined by subtracting or adding the square root of the number of particles counted in each size bin. This technique represents uncertainty in the actual particle counts for each size bin as given by Poisson statistics (Hallett, 2003; McFarquhar et al., 2007a).

Figure 3 illustrates the frequency distribution of the ratio between $\chi^2_{\min}$ and $\Delta\chi^2_1$ for all 16 flight legs. Of all 16 legs considered, 15 have a ratio greater than 1, meaning $\chi^2_{\min} > \Delta\chi^2_1$ and $\Delta\chi^2 = \chi^2_{\min}$, and 50% of the observations have ratios greater than 10. This indicates that the $\chi^2$ obtained from the $(a,b)$ minimization procedure is greater than the difference between moments derived from the minimum and maximum $N(D)$ for nearly all periods in this study. This means that the natural parameter variability over a flight leg is typically more important for the uncertainty of $m$-$D$ coefficients than is the uncertainty due to statistical counting. This is further discussed in Sect. 5.

At first, the $b$ coefficients greater than 3 shown in Fig. 2 may seem counter intuitive as the mass of a particle cannot be greater than that of an ice sphere. Further, a particle's density would increase with increasing $D$ for $b > 3$. But, due to the covariability of $a$ and $b$, $b > 3$ does not necessarily imply the particle has a mass greater than a sphere. Nevertheless, equally plausible $b$ values greater than 3 were closely inspected as past studies (e.g., Fontaine et al., 2014) have disregarded $b > 3$ as a possible exponent in an $m$-$D$ relation. To investigate the impact of $b > 3$, a linear sequence of $b$ values in the plausible surface was generated for each flight leg and the 5th, 25th, 50th, 75th, and 95th percentiles of $b$ were determined. The corresponding $a$ from each of these $b$ was identified, and the cumulative reflectivity distribution functions, defined as

$$
Z_c(D) = \left(\frac{6}{\pi \times \rho_{\text{ice}}}\right)^2 \frac{|K_{\text{ice}}|^2}{|K_w|^2} \int_0^D (aD'^b)^2 \, N(D') \, dD', \tag{5}
$$

were computed using the mean $N(D)$ for the period and the particle mass derived with these $a$ and $b$. Figure 4 shows an example of the $Z_c(D)$ over the range of particle sizes observed from the -23 °C flight leg on 20 May 2011 using these $a$ and $b$ coefficients. Although the $Z_c(D)$ derived using the BF95 coefficients is also shown for reference, it is worth noting that the

BF95 coefficients may reasonably resolve the particle mass for *some* particle sizes for the PSD depicted in Fig. 4. While the lower values of $a$ and $b$ yield larger $Z_c(D)$ for smaller $D$ than do the larger values of $a$ and $b$, the derived total reflectivity $Z_t = \int_{D_{min}}^{D_{max}} Z(D)\, dD$ for the $5^{th}$ and $95^{th}$ percentiles of $b$ are within 9.18 $\mathrm{mm^6\ m^{-3}}$ of the mean matched radar $Z$ of 18.36 $\mathrm{mm^6\ m^{-3}}$ (12.64 dBZ), a difference of 50 percent of the mean. In contrast, the difference of the mean from the $Z_t$ computed with BF95 is much higher, 88.6%, suggesting values of $b > 3$ are indeed giving plausible results for the range of particle sizes observed.

When the six flight legs that have some values of $b > 3$ in the surface of equally plausible solutions are considered, $Z$ values for the $5^{th}$ and $95^{th}$ percentiles of $b$ are within 82.4% of the mean matched radar $Z$. While this value is greater than the 50.5% difference for the other flight legs and for the period illustrated in Fig. 4, $Z$ values for the $5^{th}$ and $95^{th}$ percentiles are more consistent with the mean matched radar $Z$ compared to that computed with BF95.

Thus, the bulk variables such as $Z$ derived using $b > 3$ are physically plausible for the distributions examined here given the covariability of $a$ and $b$. However, this conclusion may only apply when the coefficients are applied over the range of particle sizes observed during MC3E and assuming PSDs with similar shapes. For example, for the $95^{th}$ percentile of $b$ ($b = 3.32$) and the corresponding value of $a$ used to construct Fig. 4, ice particles with $D < 85$ cm have particle masses less than those of spherical particles with a density of solid ice for the same maximum dimension. On the other hand, if the covariability of $a$ and $b$ was not taken into account when choosing the corresponding $a$ value, then a particle could have a mass greater than that of a spherical particle for much smaller $D$. While the technique highlights the possibility of a wide range of *m-D* coefficients for a given environment, equally plausible solutions containing $b > 3$ are still not considered in this study to remain consistent with previous studies and to avoid any chance of unphysical behavior should the equally plausible coefficients be applied to PSDs from remote sensing retrievals or microphysics parameterization schemes that extend to particle sizes larger than in the original dataset.

## 4   Events overview

The Citation aircraft sampled different ice phase environments during the 25 April, 20 May, and 23 May 2011 flights. Jensen et al. (2016) provide an overview of all MC3E cases, while Jensen et al. (2014) give a synoptic scale overview of the MCSs examined in this study. Figure 5 shows a 0.5° plan-position indicator (PPI) scan of corrected radar reflectivity from the KVNX radar for each event. The PPI was obtained during the middle of the UND Citation flight leg depicted by the black line in Fig. 5.

The first event involved an upper-level trough that produced ascent aloft and generated thunderstorms across northern Oklahoma around 06 UTC on 25 April 2011. As these storms traversed northward along an elevated frontal boundary overnight, their bases decoupled from the boundary layer as daytime solar radiation ceased. The discrete cells evolved into an MCS and moved into southern Kansas by 11 UTC (Fig. 5a) when the Citation sampled weaker embedded convection and broader stratiform precipitation. The second MCS, with a north-to-south oriented squall line which was part of a larger system, developed from a line of convective cells originating in west Texas along a dry line around 10 UTC on 20 May 2011 and propagated into the deployment region in north central Oklahoma. The Citation aircraft primarily flew within the trailing stratiform region of

the MCS (Fig. 5b). The third MCS originated as a series of discrete supercell thunderstorms along a surface dry line in western Oklahoma and moved eastward into the MC3E domain by 21 UTC on 23 May 2011 before transitioning to a more linear MCS feature. Microphysical measurements were made in the anvil region of these strong thunderstorms (Fig. 5c).

To provide context of the bulk characteristics sampled during each event, boxplots of $Z$ matched at the aircraft's location
5  and $TWC$ from the Nevzorov probe for each constant-temperature flight leg are given in Fig. 6. The whiskers represent the
$5^{th}$ and $95^{th}$ percentiles from coincident observations, the box edges denote the $25^{th}$ and $75^{th}$ percentiles, and the red line in
the middle is the median. Distributions are listed in order of decreasing temperature, with instances of multiple legs having
the same average temperature shown in chronological order. While the bulk $TWC$ and $Z$ may differ for flight legs of similar
average temperature on a given day, as in the -26.5 and -35 °C environments on 25 April (Figs. 6a-b), greater or smaller $TWC$
10  correlates with greater or smaller $Z$ for most cases. The variability in the $TWC$ and $Z$ as it relates to the construction of surfaces
of equally plausible $m$-$D$ coefficients is discussed in the next section.

## 5   Results

This section discusses how the $(a,b)$ surfaces vary between different cases, as a function of temperature, depending on the
determination of radar reflectivity, and depending on whether PSDs had large mass contributions from particles with $D > 4$
15  mm.

### 5.1   Radar absolute $Z$ calibration

While S-band radars within the NEXRAD WSR-88D network are calibrated individually and among one another upon initial
installation, biases in $Z$ can develop over time (Ice et al., 2017). Zhang et al. (2013) described a technique that uses self-
similarity in the $Z$, $Z_{DR}$, and specific differential phase ($K_{DP}$) fields to estimate the absolute $Z$ bias for events in rain. This
20  method was employed for the cases in this study and biases in $Z$ of -1.08 (25 April), -0.65 (20 May), and 1.43 dBZ (23 May
2011) were found. These corrections were applied to the value of $Z$ calculated as explained in Sect. 3. The surfaces of $m$-$D$
coefficients derived using the matched radar $Z$ and that with the bias corrections applied were similar, with the range of equally
plausible $b$ values differing, on average, by 6.4% after the corrections were made.

### 5.2   Accounting for mass contributions from larger particles

25  As discussed in Sect. 2.3.2, the Nevzorov probe is prone to larger particles ($D > 4$ mm) bouncing out of the collection cone
resulting in potential $TWC$ underestimations. Mass contents were derived from the PSDs using BF95's $m$-$D$ relation to identify
time periods in which the contribution of mass from particles with $D > 4$ mm was likely greater than 20%. Of all 10 s PSDs
used in this study, 20.9% had mass contributions from these larger particles exceeding 20% of the total mass. Figure 7 illustrates
the similarity in the $(a,b)$ surfaces generated using all coincident observations (red shading) and only those using observations
30  with mass from larger particles contributing $\leq$ 20% of the total mass (blue shading) for the 23 May 2011 event. Regions of
overlap between the two approaches only appear as blue shading. The sensitivity test shows that omitting observations where

larger particles contribute fractionally more to the total mass yield an area of equally plausible (*a*,*b*) surfaces for the 23 May event differing, on average, by 1.4% and as such all coincident observations are used for this study irrespective of the fractional contributions of particles with $D > 4$ mm to the mass.

### 5.3    Environmental impact on *m-D* coefficients

5    Surfaces of equally plausible *m-D* coefficients in (*a*,*b*) phase space from all flight legs outlined in Table 1 are shown in Fig. 8. For each event, flight legs are grouped by the same environmental temperature with the different colors corresponding to the time periods given in each panel. These surfaces are influenced by how *TWC* and *Z* derived from the PSDs relate to observed *TWC* and *Z*, and by the variability of each within a flight leg. The observed trends in the (*a*,*b*) surfaces and how they are affected by *N(D)*, *TWC*, and *Z* are discussed further below.

10    To compare surfaces of equally plausible solutions between different environments and also between periods with the same temperature, the percent of overlap between any two flight legs is computed and shown as a matrix in Fig. 9. The percentage of overlap is determined by counting the number of (*a*,*b*) pairs contained in both equally plausible surfaces for the conditions listed in the row and column in the matrix and dividing by the number of (*a*,*b*) pairs in the surface for the condition listed in the row multiplied by 100%. There are two values in the matrix corresponding to each comparison between two flight legs, with

15    differences between the two values resulting from dividing the area of the equally plausible surface from the corresponding column by that in the corresponding row in the matrix. Using the (*a*,*b*) surfaces from the -26.5 °C flight legs on 25 April (Fig. 8b) as an example, 62% of the (*a*,*b*) surface for the 11:05:20–11:14:45 UTC period (labeled -26.5 °C I; Fig. 9a) overlaps with the later -26.5 °C flight leg while 65% of the (*a*,*b*) surface for the 11:21:20–11:34:05 UTC period (labeled -26.5 °C II) overlaps with the earlier -26.5 °C flight leg. The difference occurs because there are 1132 (*a*,*b*) pairs in the surface for the

20    11:05:20–11:14:45 UTC period and 1077 (*a*,*b*) pairs in the surface for the 11:21:20–11:34:05 UTC period. Flight legs having the same temperature are ordered chronologically as in Fig. 8 and differentiated with a Roman numeral. Differences of the (*a*,*b*) surfaces between flight legs are further discussed below.

#### 5.3.1    25 April case

While differences exist between the (*a*,*b*) surfaces for the near-constant temperature legs on 25 April (Fig. 9a), these surfaces

25    have considerable overlap with each other for $a < 0.01$ g cm$^{-b}$ and $b < 2.5$ (Figs. 8a-c). The -22 and -26.5 °C legs have similar sets of equally plausible solutions, with (*a*,*b*) surfaces overlapping between 44 and 90% (Fig. 9a). Less agreement in the (*a*,*b*) surfaces is observed among the -35 °C flight legs, with the surfaces overlapping on average 23.4% among the different combinations. The differences in the size of the surfaces is primarily influenced by the natural variability within cloud because $\chi^2_{min} > \Delta\chi^2_1$ as shown in Sect. 3. The areas of the (*a*,*b*) surfaces for the -22 and -26.5 °C legs were, on average, 37.5% smaller

30    than the surfaces associated with the -35 °C environment (Figs. 8a-c). Three of the four -35 °C legs have surfaces larger than the -22 and -26.5 °C environments as the surface of equally plausible *m-D* coefficients extends beyond the maximum value *a* of 0.014 g cm$^{-b}$ and *b* of 2.88 found for the -22 and -26.5 °C legs. To explain the variation of these (*a*,*b*) surfaces for the different temperatures, the distributions of microphysical quantities for the times corresponding to these surfaces were examined.

To examine the variability in hydrometeors, particle images and distributions of bulk microphysical properties were analyzed for each flight leg. Example particle images from the HVPS-3, which provide information on the size and habit of ice phase particles with $D > 1$ mm, are plotted in Fig. 10. The pictured particles represent a subset of those imaged for the time period given and were chosen at random in an attempt to obtain a representative sample of hydrometeors. Figure 11 details the

5    distribution of number concentration $N_t$, median mass diameter $D_{mm}$, and a metric for particle sphericity obtained from the PSDs derived from the 2D-C and HVPS-3 data at each 10 s coincident observation. The whiskers and box edges are the same as in Fig. 6. Particle sphericity $\zeta$ (McFarquhar et al., 2005; Finlon et al., 2016) is defined by

$$\zeta = A^{1/2}/P, \tag{6}$$

where $A$ is the cross-sectional area directly measured by the probe and $P$ is the perimeter determined from the sum of all pixels

10    within one diode width of the edge of the particle and the diode resolution. Finlon et al. (2016) described how higher $\zeta$ denotes more-circular particles. Sphericity values shown in Fig. 11 represent a mass-weighted mean of $\zeta$ for all particles using mass estimated from the BF95 relation within each 10 s observation. Figures 10 and 11 are ordered in the same manner as in Fig. 6, with instances of multiple legs having the same average temperature shown in chronological order.

As evidenced by the particle images at T = -22 and -26.5 °C (Figs. 10a-c), the presence of aggregates exceeding 5 mm

15    is more common compared to lower temperatures (Figs. 10d-g) where the ice crystals and aggregates appear to be skewed towards smaller sizes. Distributions of $D_{mm}$ (Fig. 11b) and $TWC$ (Fig. 6b) also indicate this trend, with a median $D_{mm}$ for the 11:05:20–11:14:45 UTC (T = -26.5 °C) flight leg of 2.2 mm while the -35 °C periods have median $D_{mm}$ ranging between 1.1 and 1.7 mm.

To illustrate that the range of equally plausible $(a,b)$ coefficients are explained by the variability of cloud parameters, the

20    distributions of bulk microphysical variables, $TWC$, and $Z$ are compared between the 11:05:20–11:14:45 UTC (T = -26.5 °C) and 10:03:05–10:08:45 UTC (T = -35 °C) periods. The -26.5 °C flight leg had ranges in $N_t$, $D_{mm}$, sphericity, $Z$, and $TWC$ between the 25th and 75th percentiles (interquartile range hereafter) of 21.5 L$^{-1}$, 1.3 mm, 0.04, 5.2 dBZ, and 0.73 g m$^{-3}$, respectively, while the same variables for the -35 °C period had smaller interquartile ranges of 7.4 L$^{-1}$, 0.1 mm, 0.02, 4.0 dBZ, and 0.17 g m$^{-3}$ (Figs. 6a,b; 11a-c). The distribution of $\chi^2$ in $(a,b)$ phase space is expected to differ when the variability

25    in $N(D)$ throughout a flight leg is different between two periods since different $a$ and $b$ are likely to yield $TWC_{SD}$ and $Z_{SD}$ similar to the observed $TWC$ and $Z$. Figure 12 illustrates the distribution of $\chi^2$ for the two periods, with the outlined region representing $\chi^2$ values that are $\leq 2$ for comparison. The region containing $\chi^2 \leq 2$ is 90.8% smaller for the -26.5 °C flight leg compared to the -35 °C period and indicates that the $TWC_{SD}$ and $Z_{SD}$ derived from all possible $a$ and $b$ remain fairly consistent over the course of the -26.5 °C flight leg due to the smaller interquartile ranges in the $TWC$, $Z$, and bulk microphysical properties. As

30    such, low $\chi^2$ values are present over a larger range of $m$-$D$ coefficients for the -35 °C leg.

Although the distribution of $\chi^2$ is an important factor in determining the surface of equally plausible $m$-$D$ coefficients, the $\Delta\chi^2$ confidence region, which is equal to $\chi^2_{min}$ for 15 of the 16 flight legs (Sect. 3), also influences the $(a,b)$ surfaces. While the allowable tolerance is a factor of 2 greater for the -26.5 °C leg, the equally plausible $(a,b)$ surface is 3.4 times smaller compared to the -35 °C flight leg (Figs. 8b,c) because of the magnitude and distribution of $\chi^2$ values in $(a,b)$ phase space. Put

another way, more $\chi^2$ values considered within the ($a,b$) phase space are greater than the $\chi^2_{\min} + \Delta\chi^2$ criteria to be considered equally plausible solutions compared to the -35 °C leg.

### 5.3.2 20 May case

The wide range of temperatures sampled during the 20 May event was associated with a large variation in $Z$ (Fig. 6c), with median values ranging between 12.5 dBZ (T = -23 °C) and 27.1 dBZ (T = -5.5 °C). Representative particle images (Fig. 13) highlight differences in particle size and habit between the higher temperature flight legs (T = -5.5 and -10.5 °C) and the lower temperature periods (T = -16 and -23 °C), with images from the -5.5 and -10.5 °C legs indicating a greater frequency of larger ice crystals and aggregates with $D \geq 2$ mm. A Mann-Whitney U test confirms that $D_{mm}$ (Fig. 11e) and sphericity (Fig. 11f) between the higher and lower temperature environments are statistically different at the 99% confidence level, with notably larger and less spherical particles observed during the -5.5 and -10.5 °C flight legs. Further, median $Z$ for the -5.5 and -10.5 °C periods (22.3–27.1 dBZ) are up to 30.7 times greater than for the -16 and -23 °C legs (12.2–12.5 dBZ) while the median $TWC$ are up to 1.9 times (0.3 g m$^{-3}$) greater for the -5.5 and -10.5 °C legs. Thus, the difference in particle properties and bulk properties $TWC$ and $Z$ can be used to explain differences in ($a,b$) coefficients observed between the legs on this day.

Microphysical properties such as the effective density $\rho_e$ of ice hydrometeors can impact $TWC$ differently than they do $Z$. The $\rho_e$, defined here as the ratio of $TWC$ derived assuming the BF95 relationship to the integrated volume of particles assuming an aspect ratio of 0.6 (Hogan et al., 2012), is estimated to evaluate its influence on $TWC$ and $Z$. Median $\rho_e$ ranges between 0.05 and 0.08 g cm$^{-3}$ for the -5.5 and -10.5 °C periods and between 0.18 and 0.21 g cm$^{-3}$ for the -16 and -23 °C flight legs. These trends along with minimal riming evident from the 2D-C particle images suggest that particles are on average less compact for the higher temperature legs. Further, the presence of larger aggregates as suggested by greater values of $D_{mm}$ (Fig. 11e), lower sphericity (Fig. 11f) and $\rho_e$, and the representative particle images from the HVPS-3 (Figs. 13a,b) are consistent with increasing $Z$ when observed by longer wavelength radars (e.g., Giangrande et al., 2016).

Since differences in $\rho_e$ appear to affect the $TWC$ and $Z$ on 20 May, the variability in $N(D)$ is not the only factor influencing the equally plausible ($a,b$) surfaces depicted in Figs. 8d-g. Figure 9b illustrates that only the -16 and -23 °C legs have similar ($a,b$) surfaces, with 78% of the ($a,b$) coefficients from the -16 °C leg overlapping with the -23 °C flight leg. Minimum values of $b$ for the -5.5 and -10.5 °C flight legs, where less compact particles were observed, were 2.36 and 2.09, respectively, while minimum $b$ for the -16 and -23 °C legs were 1.74 and 1.51 for similar $a$ (Figs. 8d-g). Looking at the ($a,b$) surfaces another way, values of $a$ for the -5.5 and -10.5 °C legs were as large as 0.016 g cm$^{-b}$ while $a$ exceeds 0.05 g cm$^{-b}$ for $b = 3$ during the -16 and -23 °C flight legs. The extent of these surfaces in ($a,b$) phase space yields an area for the -5.5 and -10.5 °C flight legs that is on average 5.6 times smaller than the the -16 and -23 °C periods. When considering the $m = aD^b$ relation whose size $D$ and exponent $b$ are held fixed, lower values of $a$ as observed during the -5.5 and -10.5 °C legs suggest that particles on average have smaller $m$ compared to the -16 and -23 °C legs and are consistent with smaller $\rho_e$ observed for the -5.5 and -10.5 °C periods.

### 5.3.3 23 May case

The 23 May case was unique from the other two cases in that the bulk $Z$ varied less between the different temperature environments (Fig. 6e), with median $Z$ ranging only between 16.9 and 18.2 dBZ. Representative particle images (Fig. 14) in addition to distributions of $D_{mm}$ (Fig. 11h) and sphericity (Fig. 11i), with median values of each varying by 0.4 mm and 0.04 respectively,

5   indicate that the sizes and shapes of ice hydrometeors are also similar for all five flight legs. Equally plausible $(a,b)$ surfaces were also similar irrespective of temperature (Figs. 8h,i), with the four flight legs after the 21:49:55–21:55:15 UTC period having surfaces that overlap on average 56.1% among the different combinations (Fig. 9c). The 21:49:55–21:55:15 UTC leg is the only period where its $(a,b)$ surface has minimal overlap with the other equally plausible surfaces. Closer examination of the bulk $TWC$ (Fig. 6f) indicates that values at the fifth percentile for the 21:49:55–21:55:15 UTC period are 65.2% less than the

10  remaining flight legs, which impacts the distribution of $\chi^2$ values and the $(a,b)$ values that are within the $\chi^2_{\min} + \Delta\chi^2$ threshold.

Although surfaces of equally plausible solutions trend larger in area for lower temperature environments on 25 April and 20 May, the area of $(a,b)$ surfaces among the five flight legs on 23 May are on average 6.8 (6.4) times smaller compared to the 25 April (20 May) event. To examine how the distribution of $\chi^2$ in $(a,b)$ phase space is affected by differences in the variability of $TWC$ and $Z$ throughout a flight leg, the 14:16:30–14:32:15 UTC period on 20 May and the 21:49:55–21:55:15 UTC period

15  on 23 May are compared because of their similar temperature and $\chi^2_{\min} + \Delta\chi^2$ threshold used to determine the $(a,b)$ surfaces. Figure 15 illustrates the distribution of $\chi^2$ for the two periods, with the outlined region representing $\chi^2$ values that are $\leq 1$ for the purpose of comparison. The region containing $\chi^2 \leq 1$ is 88.2% smaller for the 23 May flight leg compared to the 20 May period, and highlights how different $a$ and $b$ can yield a $\chi^2$ value that is within the given tolerance based on differences in the observed $TWC$ and $Z$ distributions. When bulk $TWC$ and $Z$ are compared against the 25 April (20 May) events, the median $Z$

20  from flight legs on 23 May is on average 34.4% (25.9%) lower while the median TWC is 90.3% (43.9%) greater. As mentioned in Sect. 4, the sampling strategy on 23 May was different from the stratiform clouds observed with the previous two events in that measurements were primarily made in the anvil region of supercell thunderstorms. Previous studies (e.g., Heymsfield et al., 2007) noted that the prefactor $a$ had less of a temperature dependence within anvil cirrus clouds, consistent with trends in $a$ for the 23 May flight legs.

## 6 Conclusions

This paper presented a novel approach to characterize the variability of mass-Dimension ($m$-$D$) coefficients characterizing particle size distributions (PSDs) during the Mid-latitude Continental Convective Clouds Experiment (MC3E). The technique outlined here extends the approach of McFarquhar et al. (2015), who derived a volume of equally realizable solutions in the phase space of gamma fit parameter coefficients to characterize PSDs. Ground-based radar measurements of reflectivity $Z$

30  from the Vance Air Force Base, OK radar were matched to the location of the Cessna Citation II aircraft where total water content ($TWC$) measurements from the Nevzorov probe were made and PSDs were derived from optical array probe data. These collocated datasets permitted use of a $\chi^2$ minimization technique where all $\chi^2$ within a tolerance $\Delta\chi^2$ of the minimum $\chi^2$ were considered equally plausible solutions to the $m = aD^b$ relationship for a flight leg of similar temperature. The tolerance

was determined by considering uncertainties due to natural variability of cloud conditions for a particular environment and the statistical sampling of particles from the PSDs.

The key findings of the paper are as follows:

1. The distribution of $\chi^2$ values in $(a,b)$ phase space shows that the $a$ and $b$ parameters are highly correlated, as expected. The distribution of how the $(a,b)$ parameters vary for a given flight leg is influenced by how the PSDs, $TWC$ from the Nevzorov probe, and $Z$ from radar vary within a flight leg of similar temperature. Flight legs that have little variability in the microphysical properties, such as the 10:03:05–10:08:45 UTC period on 25 April, occupy a surface area in $(a,b)$ phase space that is up to 10.9 times larger than flight legs where microphysical properties vary more, such as the 11:05:20–11:14:45 UTC leg on the same day.

2. Surfaces of equally plausible solutions appear dependent on temperature for the 25 April and 20 May events. The range of plausible $a$ and $b$ coefficients is larger for flight legs of lower temperature, and 80% of the surfaces compared between the lowest and highest temperature for each day overlap by less than 50%.

3. Cases with little dependence of the surfaces of equally plausible solutions on temperature, like the flight legs analyzed on 23 May, can be explained in terms of the regions of cloud sampled and the types of ice hydrometeors observed. A mean overlap of 56.1% between four of the five $(a,b)$ surfaces on that day is consistent with previous studies (e.g., Heymsfield et al., 2007) that note little dependence in the $a$ coefficient with temperature in anvil cirrus clouds.

4. The minimum $\chi^2$ in $(a,b)$ phase space determines the allowable tolerance $\Delta\chi^2$ for 15 of the 16 flight legs when determining the set of equally plausible $a$ and $b$ coefficients, meaning that the uncertainty in the $m$-$D$ coefficients is primarily driven by the natural parameter variability over a flight leg rather than the uncertainty in the PSDs due to uncertainties in sampling statistics.

5. The covariability of $a$ and $b$ permit possible solutions of $b > 3$ for the ranges of particle sizes observed in 6 of the 16 flight legs analyzed. For these flight legs this covariability means that $Z$ derived from $a$ and $b$ and the PSDs is still within 82.4% of the mean matched radar $Z$, which is marginally greater than the 50.5% difference when $b$ is not greater than 3.

6. Flight legs where the cloud particles have lower effective density $\rho_e$, such as the -5.5 and -10.5 °C flight legs on 20 May, yield minimum $b$ values in $(a,b)$ phase space as much as 0.85 larger than clouds with a higher $\rho_e$ like the -16 and -23 °C legs on the same day. These differences can be explained by the different impacts of $\rho_e$ on $TWC$ compared to $Z$.

A key finding of this study is that a range of $a$ and $b$ coefficients should be considered as equally plausible for a given environment due to the natural variability of cloud conditions, even within a similar temperature range. This variability results in a large range of $a$ and $b$ as equally plausible solutions (as indicated in this study), and explains the range in $m$-$D$ coefficients determined in past studies (Fig. 1) where $a$ coefficients can vary by 3 orders of magnitude and $b$ coefficients between 1 and 3 for measurements made in similar environmental conditions. The technique used in this study provides insight into how equally plausible $m$-$D$ coefficients can arise because the dependence of derived microphysical parameters on environmental conditions

is generally more important than measurement uncertainties based on the instruments used to collect the data. Further, it is shown that the dependence of the (*a,b*) coefficients on temperature is still notable even when considering the ranges of equally plausible solutions.

While representing *m-D* coefficients as a range of equally plausible solutions may address shortcomings of microphysical

5  parameterization schemes and remote sensing retrievals that employ a single *m-D* relationship for a given ice species or environment, caution should be taken if the results presented here are applied to ranges of particle size or environments outside of those sampled (e.g., ones with different observed habits or various degrees of riming) to develop this parameterization. The approach presented in this study can be applied to additional studies that make use of collocated radar and microphysical measurements in other cloud and meteorological environments, and improve the statistical robustness of plausible *m-D* param-

10  eters for given environmental conditions. Such studies may help to further understand how surfaces of equally plausible (*a,b*) solutions are affected by different environments and the variability of cloud conditions therein, as well as the dependence of these solutions as a function of other cloud or environmental properties.

*Code and data availability.* The radar (doi: 10.5067/MC3E/NEXRAD/DATA202) and OAP (doi: 10.5067/GPMGV/MC3E/MULTIPLE/ DATA201) data used in this study are found on the NASA GHRC MC3E data archive. The software packages used to match the radar

15  data to the aircraft's location (https://github.com/swnesbitt/AWOT) and to process the OAP data (doi: 10.5281/zenodo.1285969) are openly available as GitHub repositories. The data containing matched radar and microphysical properties (doi: 10.13012/B2IDB-6396968_V1) used in this study are archived and available online.

## Appendix A: List of variables and their descriptions

| | |
|---|---|
| $a$ | Prefactor component in mass-Dimension relationship |
| $A$ | Particle cross-sectional area |
| $b$ | Exponent component in mass-Dimension relationship |
| $\chi^2$ | Chi-square statistic for each $(a,b)$ over a flight leg |
| $\chi^2_{\min}$ | Lowest $\chi^2$ value in $(a,b)$ phase space for a flight leg |
| $\Delta\chi^2_1$ | Uncertainty in the particle size distribution due to sampling statistics |
| $\Delta\chi^2$ | Maximum value between $\chi^2_{\min}$ and $\Delta\chi^2_1$ |
| $D$ | Particle maximum dimension |
| $D_{mm}$ | Median mass diameter |
| $IWC$ | Ice water content |
| $K_{DP}$ | Specific differential phase |
| $\lvert K_{\mathrm{ice}}\rvert^2$ | Dielectric constant for ice |
| $\lvert K_w\rvert^2$ | Dielectric constant for water |
| $N(D)$ | Number distribution function |
| $N_t$ | Number concentration |
| $P$ | Particle perimeter |
| $\rho_e$ | Effective density |
| $SDP$ | Sigma differential phase |
| $T$ | Environmental temperature |
| $TWC$ | Total water content measurement |
| $TWC_{\mathrm{diff}}$ | Normalized difference between the Nevzorov $TWC$ and that derived from the $N(D)$ for a given $(a,b)$ |
| $TWC_{\mathrm{SD}}$ | $TWC$ derived from the $N(D)$ for a given $(a,b)$ |
| $\zeta$ | Particle sphericity |
| $Z$ | Radar reflectivity factor |
| $Z_c(D)$ | Cumulative reflectivity distribution function up to size $D'$ |
| $Z(D)$ | Reflectivity distribution function |
| $Z_{\mathrm{diff}}$ | Normalized difference between the radar $Z$ and that derived from the $N(D)$ for a given $(a,b)$ |
| $Z_{\mathrm{DR}}$ | Differential reflectivity |
| $Z_{\mathrm{SD}}$ | $Z$ derived from the $N(D)$ for a given $(a,b)$ |
| $Z_t$ | Derived total reflectivity from the mean $N(D)$ for a given $(a,b)$ |

*Author contributions.* JF prepared the manuscript with contributions from all co-authors. SN provided the framework for matching radar gates to an aircraft's position. WW processed particle data from the optical array probes. PZ conducted the radar bias calculations used in this study.

*Competing interests.* The authors declare that they have no conflict of interest.

5 *Acknowledgements.* This research was supported by the US Department of Energy grants DE-SC0014065 and DE-SC0016476 (through UCAR subcontract SUBAWD000397) and by the NASA Precipitation Measurement Missions grant NNX16AD80G. We thank all participants of MC3E for collecting the data used in this study.

# References

Barnes, S. L.: A Technique for Maximizing Details in Numerical Weather Map Analysis, Journal of Applied Meteorology, 3, 396–409, https://doi.org/10.1175/1520-0450(1964)003<0396:ATFMDI>2.0.CO;2, http://journals.ametsoc.org/doi/abs/10.1175/1520-0450%281964%29003%3C0396%3AATFMDI%3E2.0.CO%3B2#.WKz-Eb_dSWU.mendeley, 1964.

5  Baumgardner, D. and Korolev, A.: Airspeed Corrections for Optical Array Probe Sample Volumes, Journal of Atmospheric and Oceanic Technology, 14, 1224–1229, https://doi.org/10.1175/1520-0426(1997)014<1224:ACFOAP>2.0.CO;2, http://journals.ametsoc.org/doi/full/10.1175/1520-0426%281997%29014%3C1224%3AACFOAP%3E2.0.CO%3B2#.WKs_amkB-pI.mendeley, 1997.

Bringi, V. N. and Chandrasekar, V.: Polarimetric Doppler Weather Radar: Principles and Applications, Cambridge University Press, http://books.google.com/books?id=KvJvfP9t5Y8C, 2001.

10  Bringi, V. N., Chandrasekar, V., Balakrishnan, N., and Zrnić, D. S.: An Examination of Propagation Effects in Rainfall on Radar Measurements at Microwave Frequencies, Journal of Atmospheric and Oceanic Technology, 7, 829–840, https://doi.org/10.1175/1520-0426(1990)007<0829:AEOPEI>2.0.CO;2, http://dx.doi.org/10.1175/1520-0426(1990)007%3C0829:AEOPEI%3E2.0.CO2, 1990.

Brown, P. R. A. and Francis, P. N.: Improved Measurements of the Ice Water Content in Cirrus Using a Total-Water Probe, Journal of Atmospheric and Oceanic Technology, 12, 410–414, https://doi.org/10.1175/1520-0426(1995)012<0410:IMOTIW>2.0.CO;2, http://dx.
15    doi.org/10.1175/1520-0426(1995)012%3C0410:IMOTIW%3E2.0.CO%5Cn2, 1995.

Cazenave, F., Gosset, M., Kacou, M., Alcoba, M., Fontaine, E., Duroure, C., and Dolan, B.: Characterization of Hydrometeors in Sahelian Convective Systems with an X-Band Radar and Comparison with In Situ Measurements. Part I: Sensitivity of Polarimetric Radar Particle Identification Retrieval and Case Study Evaluation, Journal of Applied Meteorology and Climatology, 55, 231–249, https://doi.org/10.1175/JAMC-D-15-0013.1, http://dx.doi.org/10.1175/JAMC-D-15-0013.1, 2016.

20  Cotton, R. J., Field, P. R., Ulanowski, Z., Kaye, P. H., Hirst, E., Greenaway, R. S., Crawford, I., Crosier, J., and Dorsey, J.: The effective density of small ice particles obtained from in situ aircraft observations of mid-latitude cirrus, Quarterly Journal of the Royal Meteorological Society, 139, 1923–1934, https://doi.org/10.1002/qj.2058, http://onlinelibrary.wiley.com/doi/10.1002/qj.2058/full, 2013.

Delanoë, J. and Hogan, R. J.: Combined CloudSat-CALIPSO-MODIS retrievals of the properties of ice clouds, Journal of Geophysical Research, 115, D00H29–D00H29, https://doi.org/10.1029/2009JD012346, http://doi.wiley.com/10.1029/2009JD012346, 2010.

25  Erfani, E. and Mitchell, D. L.: Developing and bounding ice particle mass- and area-dimension expressions for use in atmospheric models and remote sensing, Atmospheric Chemistry and Physics, 16, 4379–4400, https://doi.org/10.5194/acp-16-4379-2016, http://www.atmos-chem-phys.net/16/4379/2016/, 2016.

Field, P. R.: Aircraft Observations of Ice Crystal Evolution in an Altostratus Cloud, Journal of the Atmospheric Sciences, 56, 1925–1941, https://doi.org/10.1175/1520-0469(1999)056<1925:AOOICE>2.0.CO;2, http://dx.doi.org/10.1175/1520-0469(1999)056%3C1925:
30    AOOICE%3E2.0.CO, 1999.

Field, P. R., Wood, R., Brown, P. R. A., Kaye, P. H., Hirst, E., Greenaway, R., and Smith, J. A.: Ice Particle Interarrival Times Measured with a Fast FSSP, Journal of Atmospheric and Oceanic Technology, 20, 249–261, https://doi.org/10.1175/1520-0426(2003)020<0249:IPITMW>2.0.CO;2, http://journals.ametsoc.org/doi/abs/10.1175/1520-0426%282003%29020%3C0249%3AIPITMW%3E2.0.CO%3B2#.WKtvq7rTK_o.mendeley, 2003.

35  Field, P. R., Heymsfield, A. J., and Bansemer, A.: Shattering and Particle Interarrival Times Measured by Optical Array Probes in Ice Clouds, Journal of Atmospheric and Oceanic Technology, 23, 1357–1371, https://doi.org/10.1175/JTECH1922.1, http://dx.doi.org/10.1175/JTECH1922.1, 2006.

Finlon, J. A., McFarquhar, G. M., Rauber, R. M., Plummer, D. M., Jewett, B. F., Leon, D., and Knupp, K. R.: A Comparison of X-Band Polarization Parameters with In Situ Microphysical Measurements in the Comma Head of Two Winter Cyclones, Journal of Applied Meteorology and Climatology, 55, 2549–2574, https://doi.org/10.1175/JAMC-D-16-0059.1, https://journals.ametsoc.org/doi/full/10.1175/JAMC-D-16-0059.1, 2016.

Fontaine, E., Schwarzenboeck, A., Delanoë, J., Wobrock, W., Leroy, D., Dupuy, R., Gourbeyre, C., and Protat, A.: Constraining mass–diameter relations from hydrometeor images and cloud radar reflectivities in tropical continental and oceanic convective anvils, Atmospheric Chemistry and Physics, 14, 11 367–11 392, https://doi.org/10.5194/acp-14-11367-2014, http://www.atmos-chem-phys.net/14/11367/2014/acp-14-11367-2014.html, 2014.

Giangrande, S. E., Toto, T., Bansemer, A., Kumjian, M. R., Mishra, S., and Ryzhkov, A. V.: Insights into riming and aggregation processes as revealed by aircraft, radar, and disdrometer observations for a 27 April 2011 widespread precipitation event, Journal of Geophysical Research: Atmospheres, 121, 5846–5863, https://doi.org/10.1002/2015JD024537, https://agupubs.onlinelibrary.wiley.com/doi/abs/10.1002/2015JD024537, 2016.

Hallett, J.: Handbook of Weather, Climate, and Water, John Wiley & Sons, Inc., Hoboken, NJ, USA, https://doi.org/10.1002/0471721603, http://onlinelibrary.wiley.com/resolve/doi?DOI=10.1002%2F0471721603.ch35#.WKnnG2yKXto.mendeley, 2003.

Helmus, J. and Collis, S.: The Python ARM Radar Toolkit (Py-ART), a Library for Working with Weather Radar Data in the Python Programming Language, Journal of Open Research Software, 4, https://doi.org/10.5334/jors.119, http://openresearchsoftware.metajnl.com/articles/10.5334/jors.119/, 2016.

Heymsfield, A.: Ice Crystal Terminal Velocities, Journal of the Atmospheric Sciences, 29, 1348–1357, https://doi.org/10.1175/1520-0469(1972)029<1348:ICTV>2.0.CO;2, http://journals.ametsoc.org/doi/abs/10.1175/1520-0469(1972)029%3C1348:ICTV%3E2.0.CO%3B2%5Cnhttp://journals.ametsoc.org/doi/pdf/10.1175/1520-0469(1972)029%3C1348:ICTV%3E2.0.CO%3B2, 1972.

Heymsfield, A. J. and Baumgardner, D.: Summary of a workshop on processing 2–D probe data, Bulletin of the American Meteorological Society, 66, 437–440, 1985.

Heymsfield, A. J., Lewis, S., Bansemer, A., Iaquinta, J., Miloshevich, L. M., Kajikawa, M., Twohy, C., and Poellot, M. R.: A General Approach for Deriving the Properties of Cirrus and Stratiform Ice Cloud Particles, Journal of the Atmospheric Sciences, 59, 3–29, https://doi.org/10.1175/1520-0469(2002)059<0003:AGAFDT>2.0.CO;2, http://dx.doi.org/10.1175/1520-0469(2002)059%3C0003:AGAFDT%3E2.0.CO, 2002.

Heymsfield, A. J., Bansemer, A., and Twohy, C. H.: Refinements to Ice Particle Mass Dimensional and Terminal Velocity Relationships for Ice Clouds. Part I: Temperature Dependence, Journal of the Atmospheric Sciences, 64, 1047–1067, https://doi.org/10.1175/JAS3890.1, http://dx.doi.org/10.1175/JAS3890.1, 2007.

Heymsfield, A. J., Schmitt, C., Bansemer, A., and Twohy, C. H.: Improved Representation of Ice Particle Masses Based on Observations in Natural Clouds, Journal of the Atmospheric Sciences, 67, 3303–3318, https://doi.org/10.1175/2010JAS3507.1, http://dx.doi.org/10.1175/2010JAS3507.1, 2010.

Heymsfield, A. J., Field, P. R., Bailey, M., Rogers, D., Stith, J., Twohy, C., Wang, Z., and Haimov, S.: Ice in Clouds Experiment—Layer Clouds. Part I: Ice Growth Rates Derived from Lenticular Wave Cloud Penetrations, Journal of the Atmospheric Sciences, 68, 2628–2654, https://doi.org/10.1175/JAS-D-11-025.1, https://journals.ametsoc.org/doi/full/10.1175/JAS-D-11-025.1, 2011.

Heymsfield, A. J., Schmitt, C., and Bansemer, A.: Ice Cloud Particle Size Distributions and Pressure-Dependent Terminal Velocities from In Situ Observations at Temperatures from 0° to -86°C, Journal of the Atmospheric Sciences, 70, 4123–4154, https://doi.org/10.1175/JAS-D-12-0124.1, http://dx.doi.org/10.1175/JAS-D-12-0124.1, 2013.

Hogan, R. J., Illingworth, A. J., and Sauvageot, H.: Measuring crystal size in cirrus using 35- and 94-GHz radars, Journal of Atmospheric and Oceanic Technology, 17, 27–37, https://doi.org/10.1175/1520-0426(2000)017<0027:MCSICU>2.0.CO;2, 2000.

Hogan, R. J., Mittermaier, M. P., and Illingworth, A. J.: The Retrieval of Ice Water Content from Radar Reflectivity Factor and Temperature and Its Use in Evaluating a Mesoscale Model, Journal of Applied Meteorology and Climatology, 45, 301–317, https://doi.org/10.1175/JAM2340.1, http://dx.doi.org/10.1175/JAM2340.1, 2006.

Hogan, R. J., Tian, L., Brown, P. R. a., Westbrook, C. D., Heymsfield, A. J., and Eastment, J. D.: Radar Scattering from Ice Aggregates Using the Horizontally Aligned Oblate Spheroid Approximation, Journal of Applied Meteorology and Climatology, 51, 655–671, https://doi.org/10.1175/JAMC-D-11-074.1, http://journals.ametsoc.org/doi/abs/10.1175/JAMC-D-11-074.1, 2012.

Ice, R. L., Richardson, L. M., Daniel, A. E., Free, A. D., Macemon, R. W., Krause, J. C., Secrest, G., Lee, R. R., Melnikov, V. M., and Hubbert, J. C.: Monitoring the Performance of the Polarimetric WSR-88D–Calibration and Sensitivity, in: 33rd Conference on Environmental Information Processing Technologies, American Meteorological Society, 2017.

Jensen, M. P., Giangrande, S. E., and Kollias, P.: The Mid-latitude Continental Convective Clouds Experiment (MC3E) Final Campaign Report, pp. 1–13, https://www.arm.gov/publications/programdocs/doe-sc-arm-14-012.pdf, 2014.

Jensen, M. P., Petersen, W. A., Bansemer, A., Bharadwaj, N., Carey, L. D., Cecil, D. J., Collis, S. M., Del Genio, A. D., Dolan, B., Gerlach, J., Giangrande, S. E., Heymsfield, A., Heymsfield, G., Kollias, P., Lang, T. J., Nesbitt, S. W., Neumann, A., Poellot, M., Rutledge, S. A., Schwaller, M., Tokay, A., Williams, C. R., Wolff, D. B., Xie, S., Zipser, E. J., Jensen, M. P., Petersen, W. A., Bansemer, A., Bharadwaj, N., Carey, L. D., Cecil, D. J., Collis, S. M., Genio, A. D. D., Dolan, B., Gerlach, J., Giangrande, S. E., Heymsfield, A., Heymsfield, G., Kollias, P., Lang, T. J., Nesbitt, S. W., Neumann, A., Poellot, M., Rutledge, S. A., Schwaller, M., Tokay, A., Williams, C. R., Wolff, D. B., Xie, S., and Zipser, E. J.: The Midlatitude Continental Convective Clouds Experiment (MC3E), Bulletin of the American Meteorological Society, 97, 1667–1686, https://doi.org/10.1175/BAMS-D-14-00228.1, http://journals.ametsoc.org/doi/10.1175/BAMS-D-14-00228.1, 2016.

Korolev, A. and Field, P. R.: Assessment of the performance of the inter-arrival time algorithm to identify ice shattering artifacts in cloud particle probe measurements, Atmospheric Measurement Techniques, 8, 761–777, https://doi.org/10.5194/amt-8-761-2015, http://www.atmos-meas-tech.net/8/761/2015/, 2015.

Korolev, A., Strapp, J. W., Isaac, G. A., and Emery, E.: Improved Airborne Hot-Wire Measurements of Ice Water Content in Clouds, Journal of Atmospheric and Oceanic Technology, 30, 2121–2131, https://doi.org/10.1175/JTECH-D-13-00007.1, http://journals.ametsoc.org/doi/full/10.1175/JTECH-D-13-00007.1#.WKtZQDVS8co.mendeley, 2013.

Korolev, A. V., Strapp, J. W., Isaac, G. A., and Nevzorov, A. N.: The Nevzorov Airborne Hot-Wire LWC–TWC Probe: Principle of Operation and Performance Characteristics, Journal of Atmospheric and Oceanic Technology, 15, 1495–1510, https://doi.org/10.1175/1520-0426(1998)015<1495:TNAHWL>2.0.CO;2, https://journals.ametsoc.org/doi/abs/10.1175/1520-0426%281998%29015%3C1495%3ATNAHWL%3E2.0.CO%3B2, 1998.

Lawson, R. P., Woods, S., and Morrison, H.: The Microphysics of Ice and Precipitation Development in Tropical Cumulus Clouds, Journal of the Atmospheric Sciences, 72, 2429–2445, https://doi.org/10.1175/JAS-D-14-0274.1, https://journals.ametsoc.org/doi/10.1175/JAS-D-14-0274.1, 2015.

Lemke, H. M. and Quante, M.: Backscatter characteristics of nonspherical ice crystals: Assessing the potential of polarimetric radar measurements, Journal of Geophysical Research: Atmospheres, 104, 31 739–31 751, https://doi.org/10.1029/1999JD900490, http://doi.wiley.com/10.1029/1999JD900490, 1999.

Leroy, D., Fontaine, E., Schwarzenboeck, A., and Strapp, J. W.: Ice Crystal Sizes in High Ice Water Content Clouds. Part I: On the Computation of Median Mass Diameter from In Situ Measurements, Journal of Atmospheric and Oceanic Technology, 33, 2461–2476, https://doi.org/10.1175/JTECH-D-15-0151.1, http://journals.ametsoc.org/doi/10.1175/JTECH-D-15-0151.1, 2016.

Liu, G. and Curry, J. a.: Determination of Ice Water Path and Mass Median Particle Size Using Multichannel Microwave Measurements, Journal of Applied Meteorology, 39, 1318–1329, https://doi.org/10.1175/1520-0450(2000)039<1318:DOIWPA>2.0.CO;2, 2000.

Locatelli, J. D. and Hobbs, P. V.: Fall speeds and masses of solid precipitation particles, Journal of Geophysical Research, 79, 2185–2197, https://doi.org/10.1029/JC079i015p02185, http://onlinelibrary.wiley.com/doi/10.1029/JC079i015p02185/abstract%5Cnhttp://onlinelibrary.wiley.com/store/10.1029/JC079i015p02185/asset/jgr14894.pdf?v=1&t=i1h8td42&s=bea840a363a286e28adb6368e5b7ef447d7e173f, 1974.

Maahn, M., Löhnert, U., Kollias, P., Jackson, R. C., and McFarquhar, G. M.: Developing and Evaluating Ice Cloud Parameterizations for Forward Modeling of Radar Moments Using in situ Aircraft Observations, Journal of Atmospheric and Oceanic Technology, 32, 880–903, https://doi.org/10.1175/JTECH-D-14-00112.1, http://dx.doi.org/10.1175/JTECH-D-14-00112.1, 2015.

Magono, C. and Nakamura, T.: Aerodynamic Studies of Falling Snowflakes, Journal of the Meteorological Society of Japan, 43, 139–147, 1965.

Maneewongvatana, S. and Mount, D. M.: It's okay to be skinny, if your friends are fat, in: 4th Annual CGC Workshop on Computational Geometry, 1999.

Mascio, J., Xu, Z., and Mace, G. G.: The Mass-Dimensional Properties of Cirrus Clouds During TC4, Journal of Geophysical Research: Atmospheres, 122, 10,402–10,417, https://doi.org/10.1002/2017JD026787, http://doi.wiley.com/10.1002/2017JD026787, 2017.

Matrosov, S. Y.: Modeling Backscatter Properties of Snowfall at Millimeter Wavelengths, Journal of the Atmospheric Sciences, 64, 1727–1736, https://doi.org/10.1175/JAS3904.1, http://journals.ametsoc.org/doi/full/10.1175/JAS3904.1%5Cnhttp://journals.ametsoc.org/doi/pdf/10.1175/JAS3904.1, 2007.

Matrosov, S. Y.: Assessment of Radar Signal Attenuation Caused by the Melting Hydrometeor Layer, IEEE Transactions on Geoscience and Remote Sensing, 46, 1039–1047, https://doi.org/10.1109/TGRS.2008.915757, 2008.

McCumber, M., Tao, W.-K., Simpson, J., Penc, R., Soong, S.-T., McCumber, M., Tao, W.-K., Simpson, J., Penc, R., and Soong, S.-T.: Comparison of Ice-Phase Microphysical Parameterization Schemes Using Numerical Simulations of Tropical Convection, Journal of Applied Meteorology, 30, 985–1004, https://doi.org/10.1175/1520-0450-30.7.985, http://journals.ametsoc.org/doi/abs/10.1175/1520-0450-30.7.985, 1991.

McFarquhar, G. M. and Heymsfield, A. J.: Microphysical Characteristics of Three Anvils Sampled during the Central Equatorial Pacific Experiment, Journal of the Atmospheric Sciences, 53, 2401–2423, https://doi.org/10.1175/1520-0469(1996)053<2401:MCOTAS>2.0.CO;2, http://dx.doi.org/10.1175/1520-0469(1996)053%3C2401:MCOTAS%3E2.0.CO, 1996.

McFarquhar, G. M., Timlin, M. S., Nousiainen, T., and Yang, P.: A New Representation of the Single-Scattering Properties for Mid-latitude Clouds and its Impacts, in: Fifteenth ARM Science Team Meeting Proceedings, http://www.arm.gov/publications/proceedings/conf15/extended_abs/mcfarquhar_gm2.pdf?id=26, 2005.

McFarquhar, G. M., Timlin, M. S., Rauber, R. M., Jewett, B. F., Grim, J. A., and Jorgensen, D. P.: Vertical Variability of Cloud Hydrometeors in the Stratiform Region of Mesoscale Convective Systems and Bow Echoes, Monthly Weather Review, 135, 3405–3428, https://doi.org/10.1175/MWR3444.1, http://dx.doi.org/10.1175/MWR3444.1, 2007a.

McFarquhar, G. M., Zhang, G., Poellot, M. R., Kok, G. L., McCoy, R., Tooman, T., Fridlind, A., and Heymsfield, A. J.: Ice properties of single-layer stratocumulus during the Mixed-Phase Arctic Cloud Experiment: 1. Observations, Journal of Geophysical Research: Atmospheres, 112, 1–19, https://doi.org/10.1029/2007JD008633, 2007b.

McFarquhar, G. M., Hsieh, T.-L., Freer, M., Mascio, J., and Jewett, B. F.: The Characterization of Ice Hydrometeor Gamma Size Distributions as Volumes in $N_0$-$\mu$-$\lambda$ Phase Space: Implications for Microphysical Process Modeling, Journal of the Atmospheric Sciences, 72, 892–909, https://doi.org/10.1175/JAS-D-14-0011.1, http://dx.doi.org/10.1175/JAS-D-14-0011.1, 2015.

McFarquhar, G. M., Baumgardner, D., Bansemer, A., Abel, S. J., Crosier, J., French, J., Rosenberg, P., Korolev, A., Schwarzoenboeck, A., Leroy, D., Um, J., Wu, W., Heymsfield, A. J., Twohy, C., Detwiler, A., Field, P., Neumann, A., Cotton, R., Axisa, D., Dong, J., McFarquhar, G. M., Baumgardner, D., Bansemer, A., Abel, S. J., Crosier, J., French, J., Rosenberg, P., Korolev, A., Schwarzoenboeck, A., Leroy, D., Um, J., Wu, W., Heymsfield, A. J., Twohy, C., Detwiler, A., Field, P., Neumann, A., Cotton, R., Axisa, D., and Dong, J.: Processing of Ice Cloud In Situ Data Collected by Bulk Water, Scattering, and Imaging Probes: Fundamentals, Uncertainties, and Efforts toward Consistency, Meteorological Monographs, 58, 11.1–11.33, https://doi.org/10.1175/AMSMONOGRAPHS-D-16-0007.1, http://journals.ametsoc.org/doi/10.1175/AMSMONOGRAPHS-D-16-0007.1, 2017.

McFarquhar, G. M., Finlon, J. A., Stechman, D. M., Wu, W., Jackson, R. C., and Freer, M.: University of Illinois/Oklahoma Optical Array Probe (OAP) Processing Software, https://doi.org/10.5281/zenodo.1285969, https://doi.org/10.5281/zenodo.1285969, 2018.

Mitchell, D. L.: Use of Mass- and Area-Dimensional Power Laws for Determining Precipitation Particle Terminal Velocities, Journal of the Atmospheric Sciences, 53, 1710–1723, https://doi.org/10.1175/1520-0469(1996)053<1710:UOMAAD>2.0.CO;2, 1996.

Mitchell, D. L. and Arnott, W. P.: A Model Predicting the Evolution of Ice Particle Size Spectra and Radiative Properties of Cirrus Clouds. Part II: Dependence of Absorption and Extinction on Ice Crystal Morphology, Journal of the Atmospheric Sciences, 51, 817–832, https://doi.org/10.1175/1520-0469(1994)051<0817:AMPTEO>2.0.CO;2, https://journals.ametsoc.org/doi/abs/10.1175/1520-0469%281994%29051%3C0817%3AAMPTEO%3E2.0.CO%3B2, 1994.

Mitchell, D. L., Zhang, R., and Pitter, R. L.: Mass-Dimensional Relationships for Ice Particles and the Influence of Riming on Snowfall Rates, Journal of Applied Meteorology, 29, 153–163, https://doi.org/10.1175/1520-0450(1990)029<0153:MDRFIP>2.0.CO;2, 1990.

Nakaya, U. and Terada, T. J.: Simultaneous Observations of the Mass, Falling Velocity and Form of Individual Snow Crystals, Journal of the Faculty of Science, Hokkaido Imperial University, 1, 191–200, http://hdl.handle.net/2115/34452, 1935.

Nevzorov, A. N.: Aircraft cloud water content meter, in: Communications a la VIIIeme Conference Internationale sur la Physique des Nuages, pp. 701–703, AIMPA, 1980.

Olson, W. S., Tian, L., Grecu, M., Kuo, K.-S., Johnson, B. T., Heymsfield, A. J., Bansemer, A., Heymsfield, G. M., Wang, J. R., and Meneghini, R.: The Microwave Radiative Properties of Falling Snow Derived from Nonspherical Ice Particle Models. Part II: Initial Testing Using Radar, Radiometer and In Situ Observations, Journal of Applied Meteorology and Climatology, 55, 709–722, https://doi.org/10.1175/JAMC-D-15-0131.1, http://dx.doi.org/10.1175/JAMC-D-15-0131.1, 2016.

Park, S.-G., Bringi, V. N., Chandrasekar, V., Maki, M., and Iwanami, K.: Correction of Radar Reflectivity and Differential Reflectivity for Rain Attenuation at X Band. Part I: Theoretical and Empirical Basis, Journal of Atmospheric and Oceanic Technology, 22, 1621–1632, https://doi.org/10.1175/JTECH1803.1, http://journals.ametsoc.org/doi/abs/10.1175/JTECH1803.1, 2005.

Schmitt, C. G. and Heymsfield, A. J.: The Dimensional Characteristics of Ice Crystal Aggregates from Fractal Geometry, Journal of the Atmospheric Sciences, 67, 1605–1616, https://doi.org/10.1175/2009JAS3187.1, http://dx.doi.org/10.1175/2009JAS3187.1, 2010.

Szyrmer, W. and Zawadzki, I.: Snow Studies. Part II: Average Relationship between Mass of Snowflakes and Their Terminal Fall Velocity, Journal of the Atmospheric Sciences, 67, 3319–3335, https://doi.org/10.1175/2010JAS3390.1, http://journals.ametsoc.org/doi/abs/10.1175/2010JAS3390.1, 2010.

Wang, J., Dong, X., and Xi, B.: Investigation of ice cloud microphysical properties of DCSs using aircraft in situ measurements during MC3E over the ARM SGP site, Journal of Geophysical Research: Atmospheres, 120, 3533–3552, https://doi.org/10.1002/2014JD022795, https://agupubs.onlinelibrary.wiley.com/doi/10.1002/2014JD022795, 2015.

Wu, W. and McFarquhar, G. M.: On the Impacts of Different Definitions of Maximum Dimension for Nonspherical Particles Recorded by 2D Imaging Probes, Journal of Atmospheric and Oceanic Technology, 33, 1057–1072, https://doi.org/10.1175/JTECH-D-15-0177.1, http://dx.doi.org/10.1175/JTECH-D-15-0177.1, 2016.

Xu, Z. and Mace, G. G.: Ice Particle Mass–Dimensional Relationship Retrieval and Uncertainty Evaluation Using the Optimal Estimation Methodology Applied to the MACPEX Data, Journal of Applied Meteorology and Climatology, 56, 767–788, https://doi.org/10.1175/JAMC-D-16-0222.1, http://journals.ametsoc.org/doi/10.1175/JAMC-D-16-0222.1, 2017.

Zhang, P., Zrnić, D., and Ryzhkov, A.: Partial Beam Blockage Correction Using Polarimetric Radar Measurements, Journal of Atmospheric and Oceanic Technology, 30, 861–872, https://doi.org/10.1175/JTECH-D-12-00075.1, http://journals.ametsoc.org/doi/abs/10.1175/JTECH-D-12-00075.1, 2013.

Zikmunda, J. and Vali, G.: Fall Patterns and Fall Velocities of Rimed Ice Crystals, Journal of the Atmospheric Sciences, 29, 1334–1347, https://doi.org/10.1175/1520-0469(1972)029<1334:FPAFVO>2.0.CO;2, 1972.
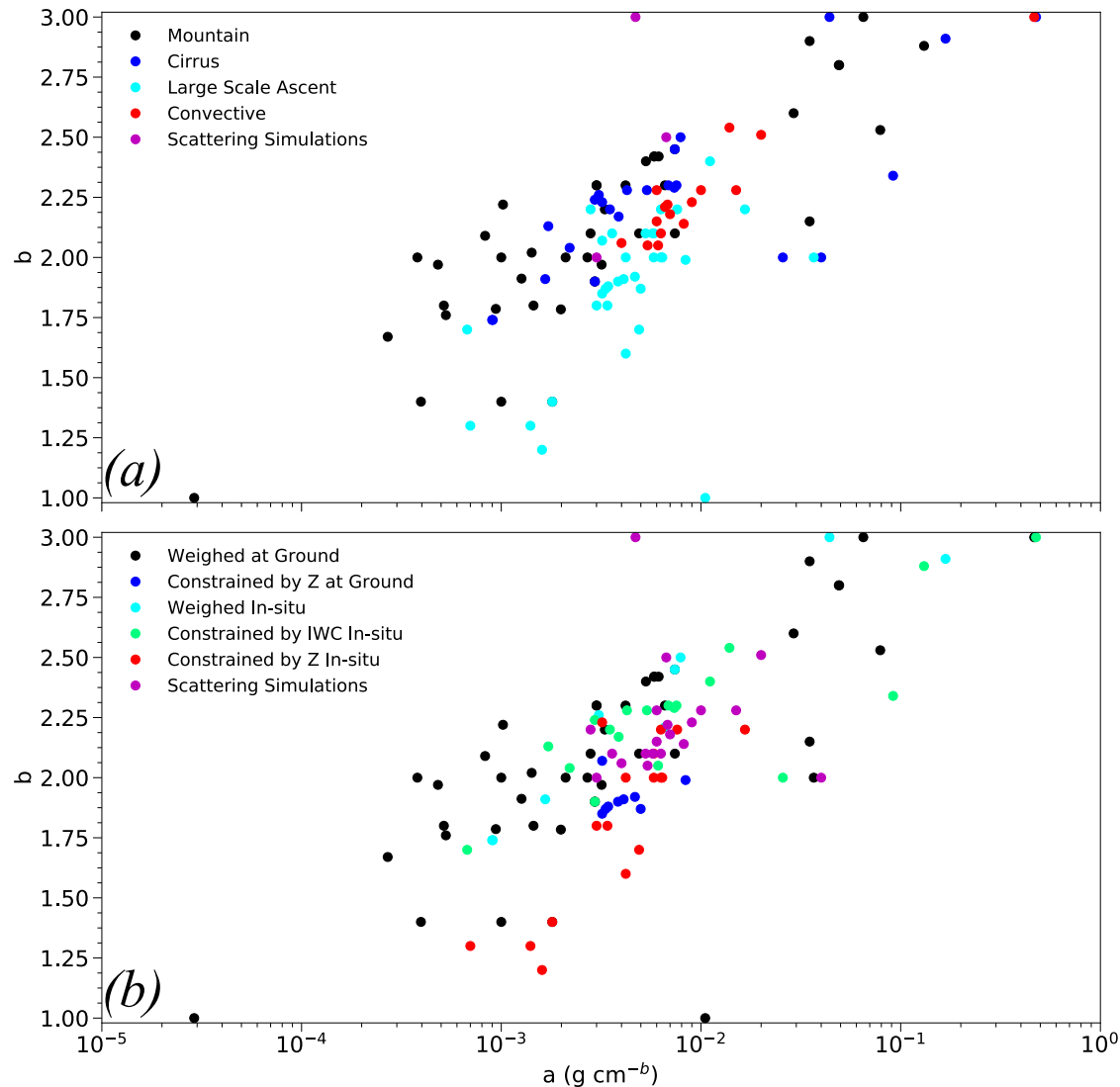
**Figure 1.** Distribution of *a* and *b* coefficients used to characterize $m = aD^b$ relationship from past studies. Points colored by the (a) environment in which measurements were made and (b) technique used to derive the relations.
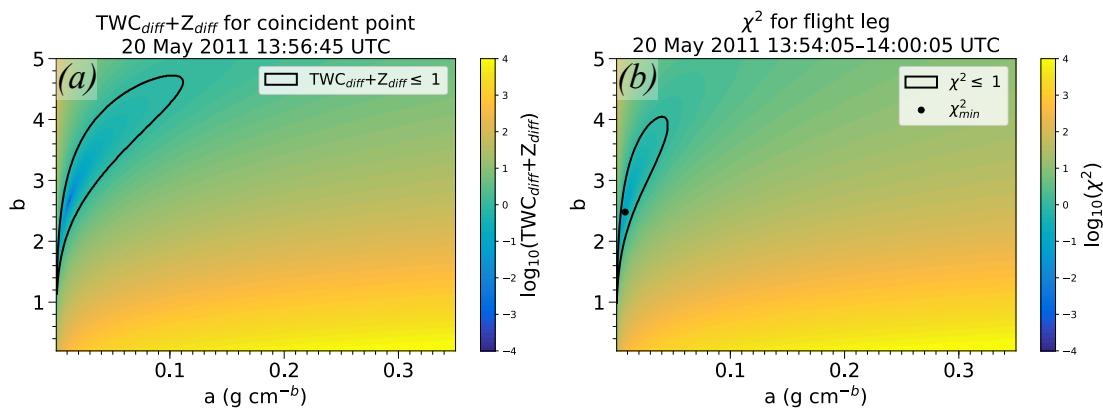
**Figure 2.** $TWC_{diff} + Z_{diff}$ in $(a,b)$ phase space for (a) a 10 s coincident point beginning 13:56:15 UTC on 20 May 2011 and (b) integrated over the encompassing flight leg between 13:54:14 and 13:59:35 UTC and normalized by the number of observations N. The black dot in (b) denotes the a and b minimizing $\chi^2$.
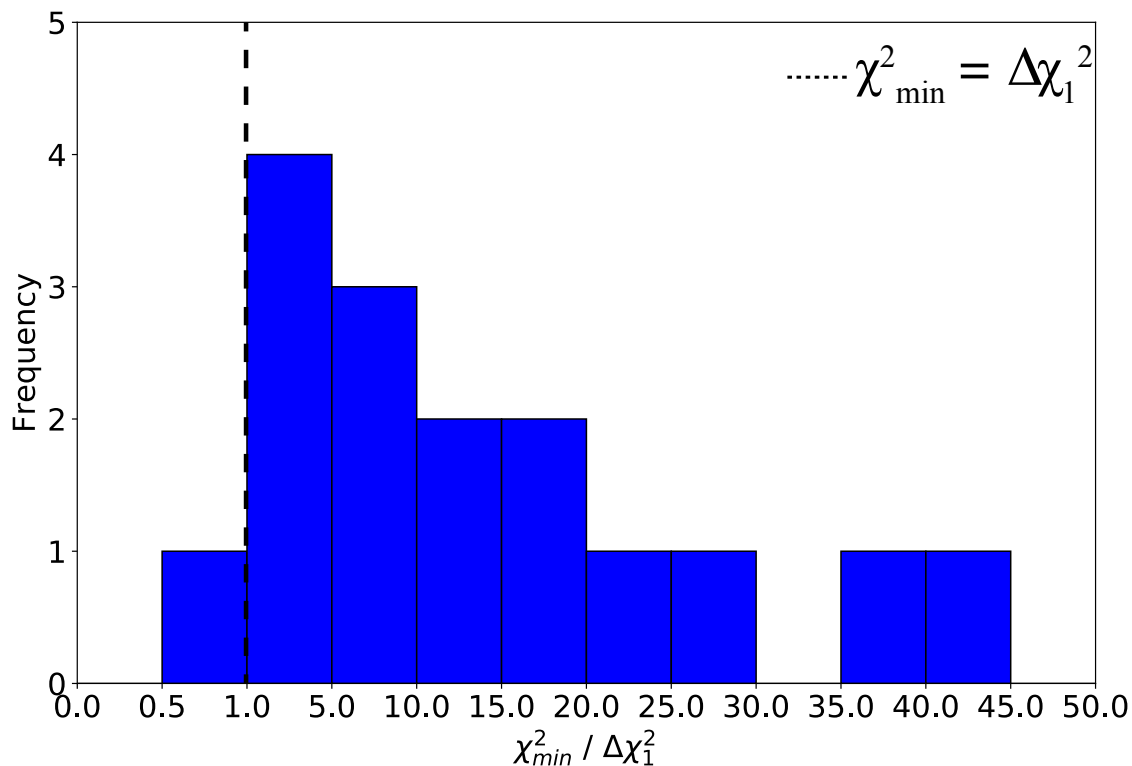
**Figure 3.** Frequency of $\chi^2_{min}/\Delta\chi^2_1$, where $\chi^2_{min}$ and $\Delta\chi^2_1$ derived for each flight leg used in analysis.
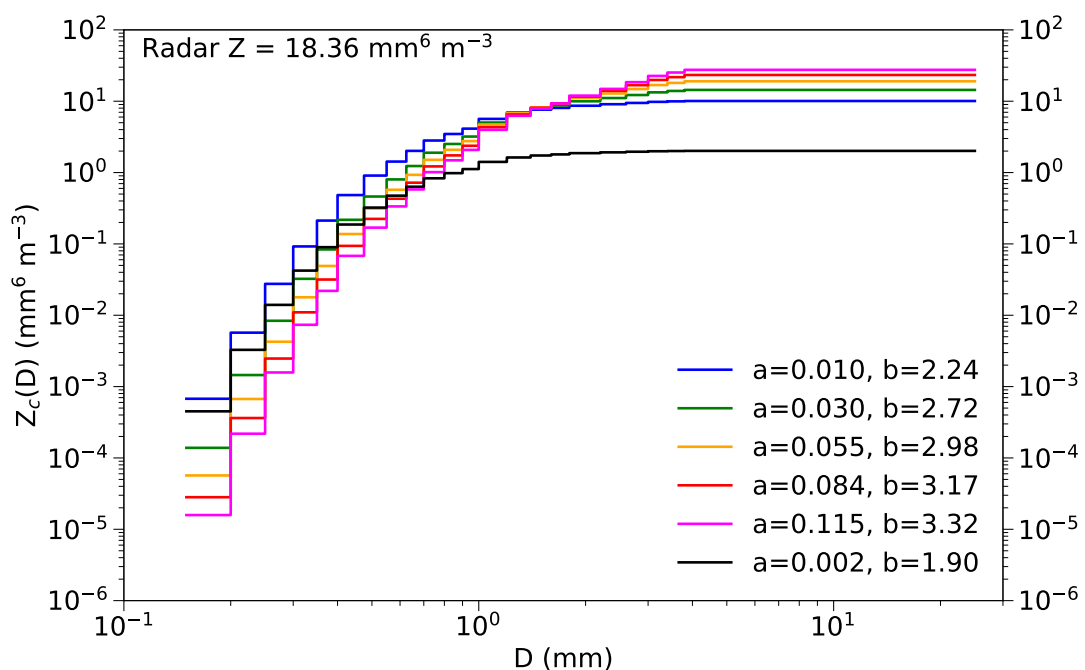
**Figure 4.** $Z_c(D)$ as a function of $D$ derived using *m-D* coefficients from BF95 (black) and from the 5th (blue), 25th (green), 50th (orange), 75th (red), and 95th (magenta) percentiles from the set of equally plausible *m-D* coefficients in order of increasing $b$ and $a$ values for the 14:16:30–14:32:15 UTC flight leg on 20 May 2011. Mean radar reflectivity matched at the aircraft's position for the same period is listed in top left.
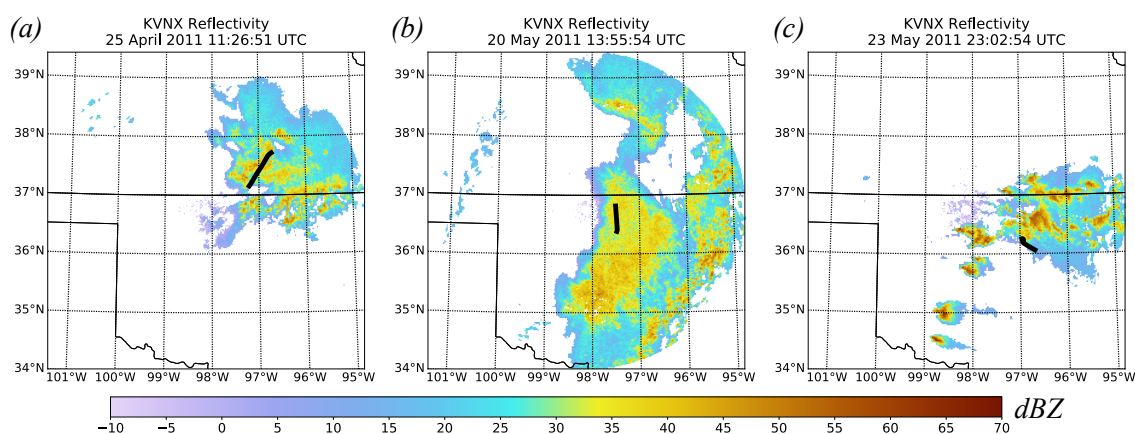
**Figure 5.** 0.5 degree PPI scan of corrected radar reflectivity from the KVNX radar for (a) 11:26:51 UTC 25 Apr 2011, (b) 14:04:34 UTC 20 May 2011, and (c) 23:02:54 UTC 23 May 2011. Black lines denote the Citation flight track for the constant-temperature leg corresponding to the radar image shown.
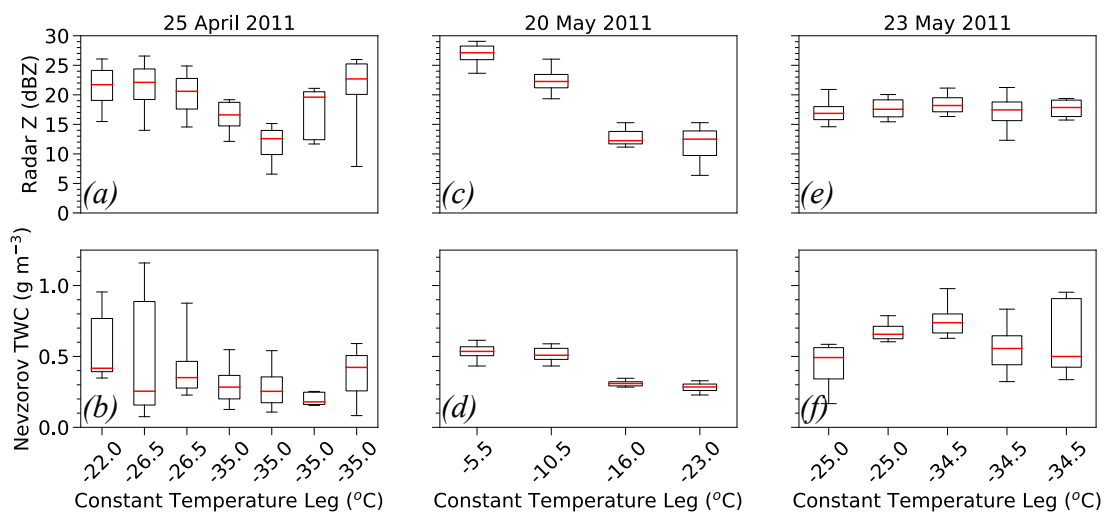
**Figure 6.** Distribution of matched *Z* (top) and *TWC* from the Nevzorov probe (bottom) for each constant-temperature leg on 25 Apr (left), 20 May (center), and 23 May 2011 (right). Whiskers represent the 5th and 95th percentiles, box edges are the 25th and 75th percentiles, and the line in the middle is the median. Cases where multiple legs of the same temperature exist are shown in chronological order.
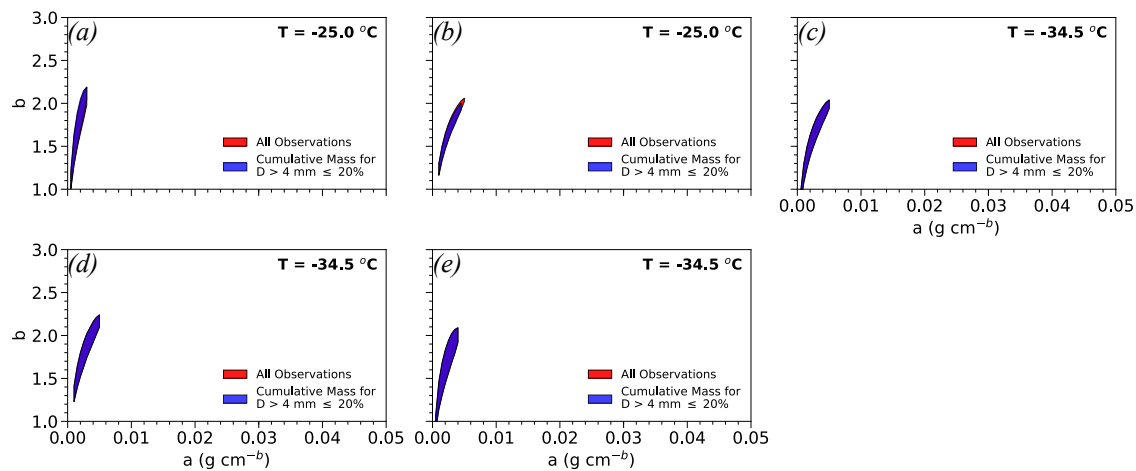
**Figure 7.** Surfaces of equally plausible $a$ and $b$ values from the $m = aD^b$ relation from each near-constant temperature leg on 23 May 2011 for all coincident observations (red) and only those where cumulative mass for $D > 4$ mm is $\leq 20$ % (blue). Flight legs of the same temperature are shown in chronological order.
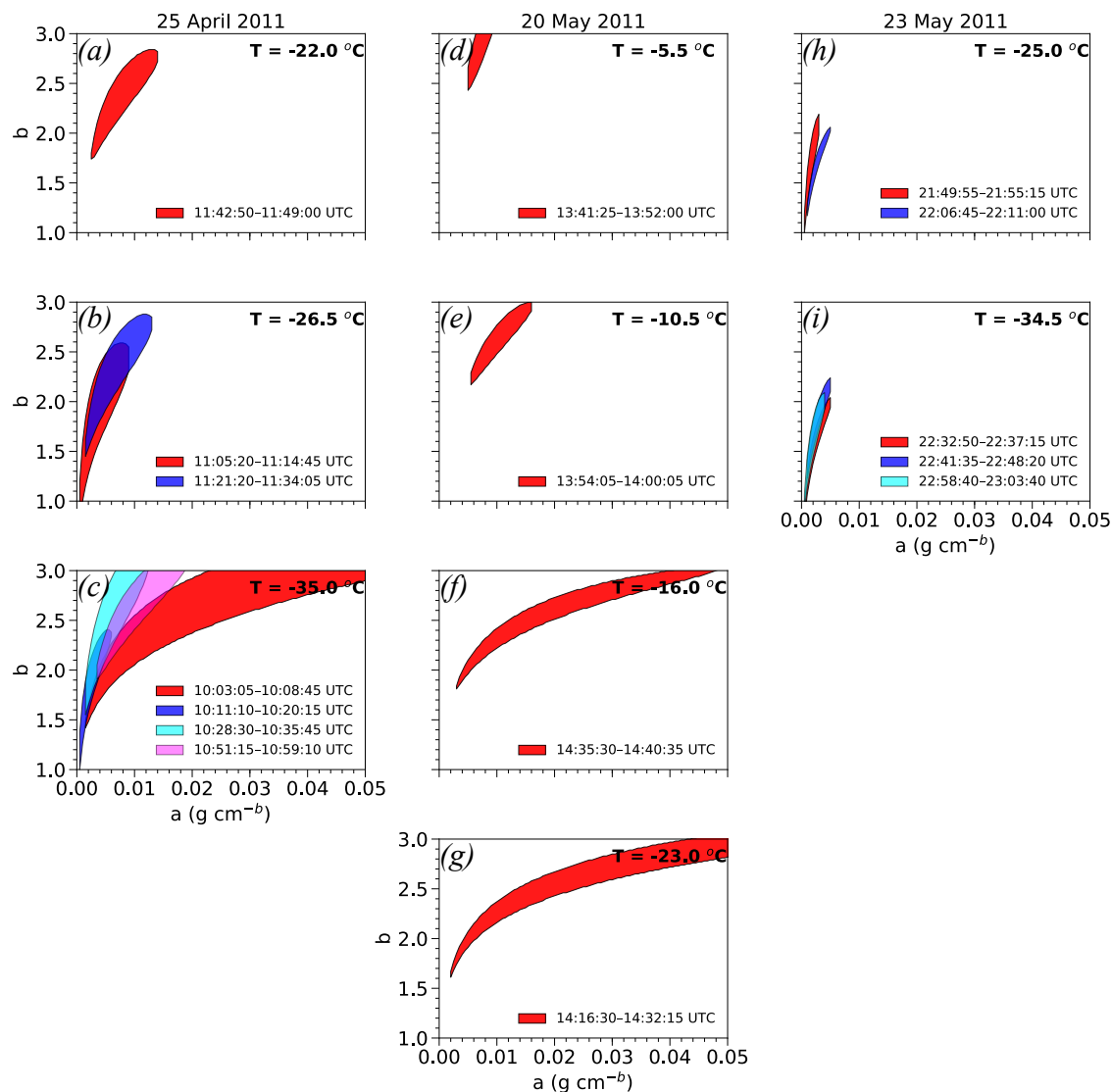
**Figure 8.** Surfaces of equally plausible *a* and *b* values for near-constant temperature flight legs for the (a–c) 25 April, (d–g) 20 May, and (h–i) 23 May 2011 events. Multiple legs occupying the same temperature are assigned a different color within a panel.
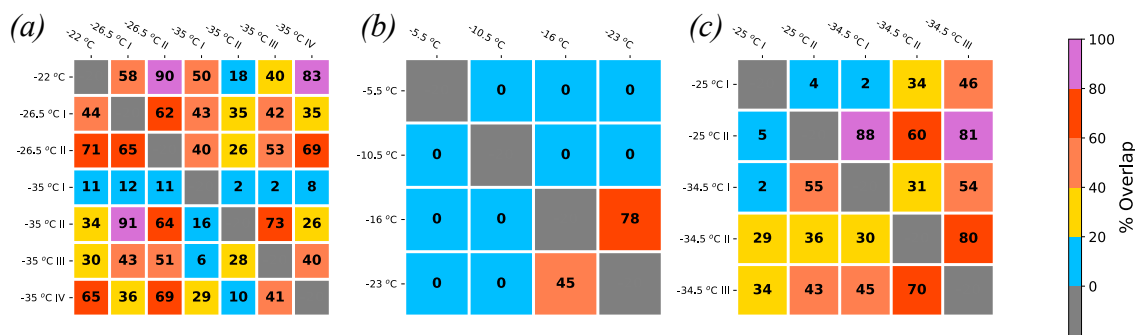
**Figure 9.** Matrix of overlap area between the equally plausible (*a,b*) surfaces corresponding to each row and column for (a) 25 April, (b) 20 May, and (c) 23 May 2011. The overlap area for each square is normalized by the area of the (*a,b*) surface corresponding to the flight leg listed in each row.
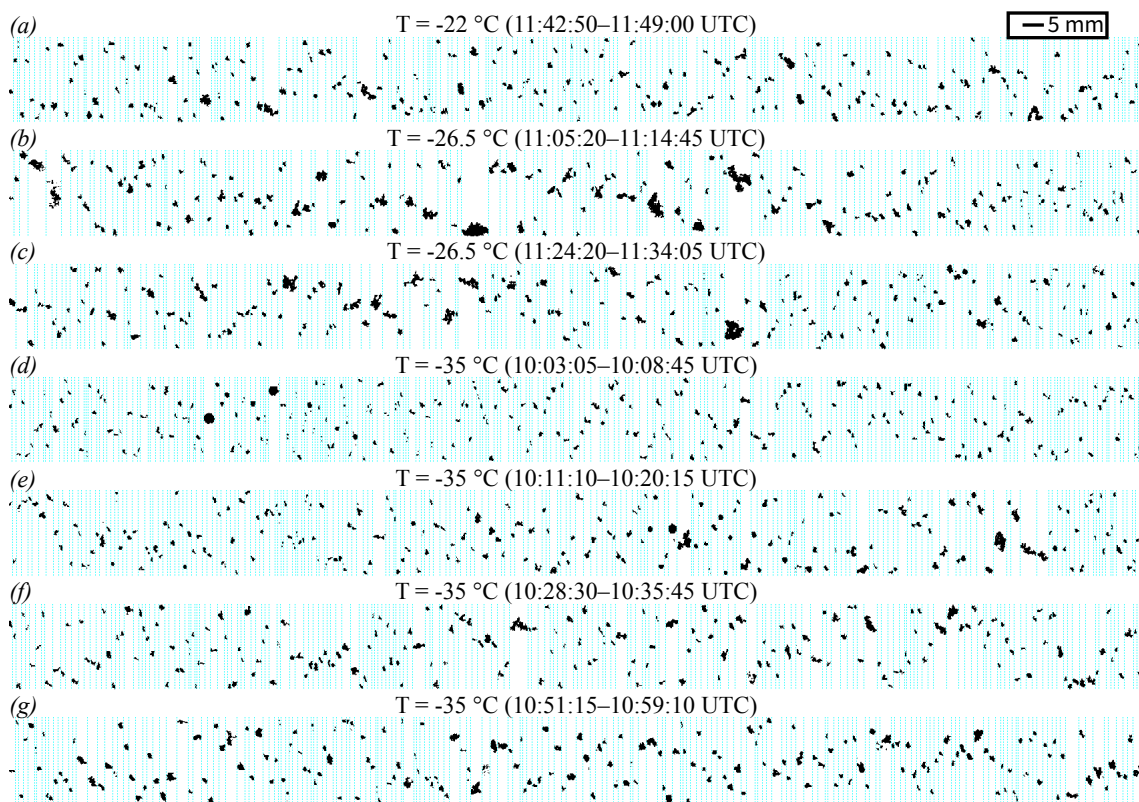
**Figure 10.** Representative particle images from the HVPS-3 for each near-constant temperature flight leg on 25 April 2011.
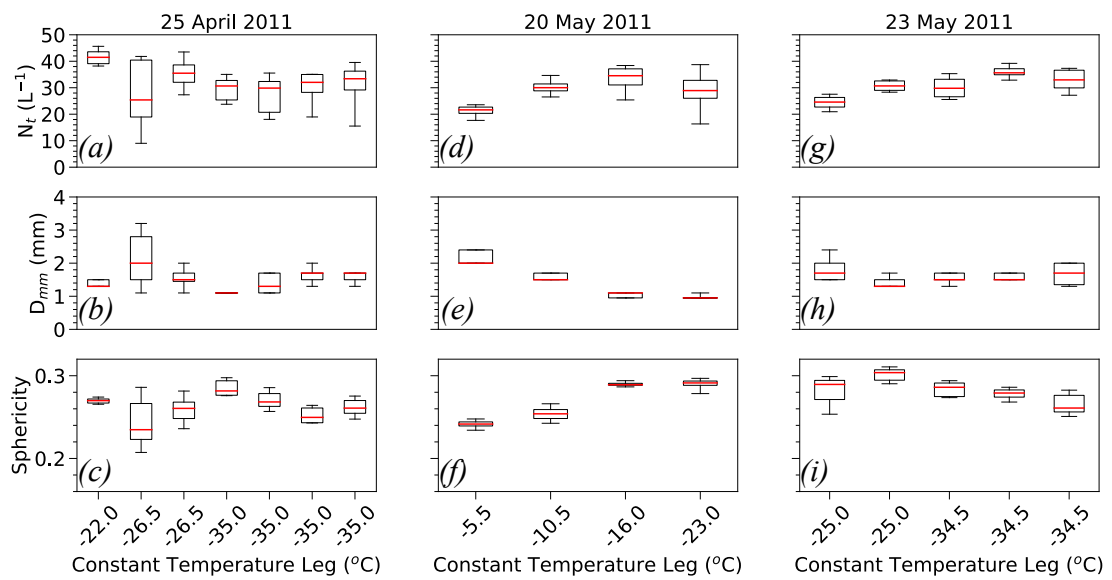
**Figure 11.** As in Fig. 6, but for number concentration $N_t$, median mass diameter $D_{mm}$, and mass-weighted mean sphericity.
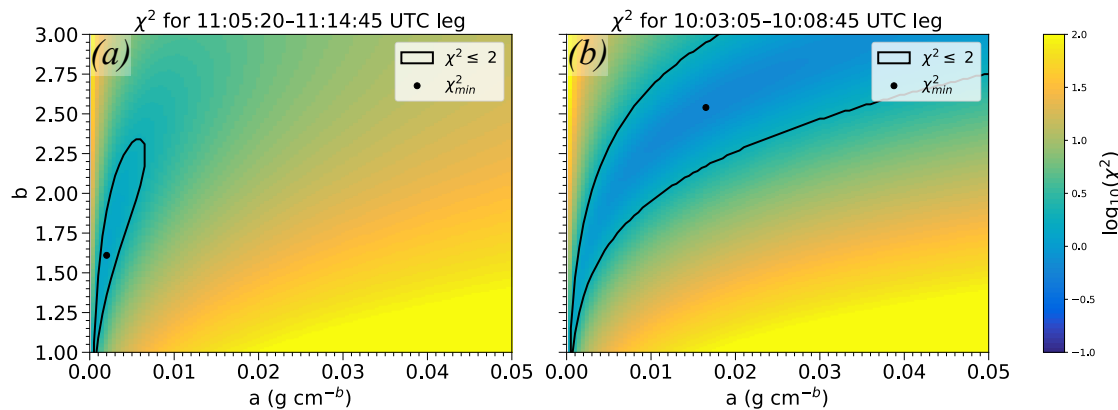
**Figure 12.** $\chi^2$ statistic in $(a,b)$ phase space for the (a) 11:05:20–11:14:45 UTC and (b) 10:03:05–10:08:45 UTC flight legs on 25 April 2011. Outlined regions represent $\chi^2 \leq 2$ and the dots $\chi^2_{min}$.
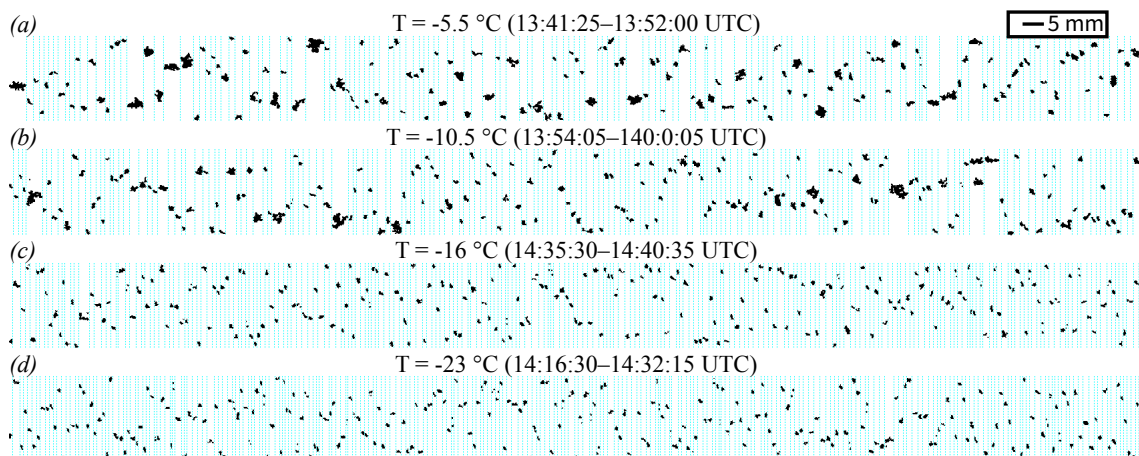
**Figure 13.** Same as in Fig. 10, but for the 20 May 2011 case.
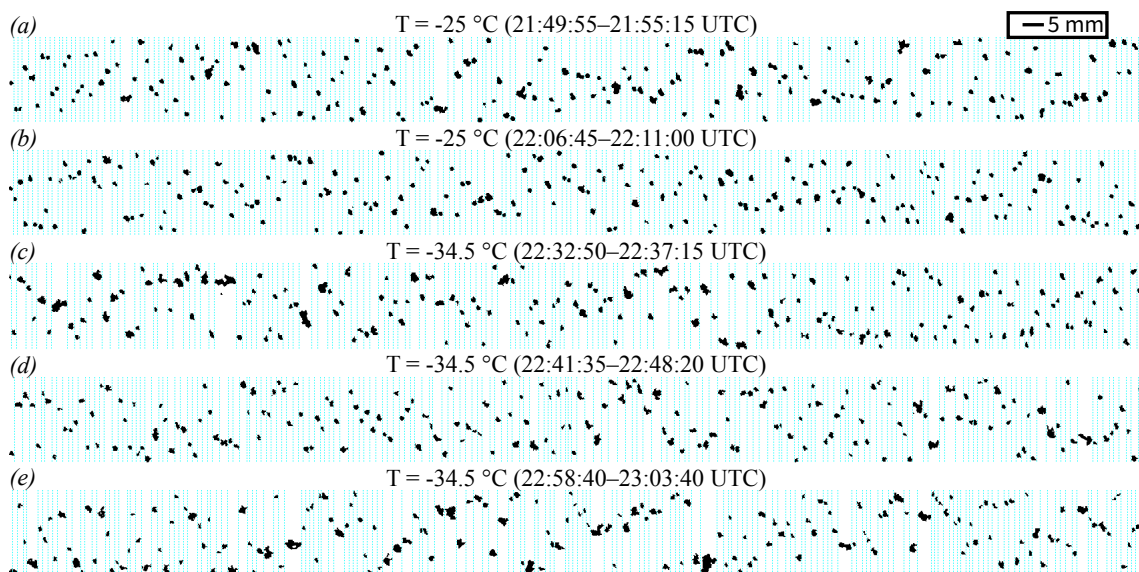
**Figure 14.** Same as in Fig. 10, but for the 23 May 2011 case.
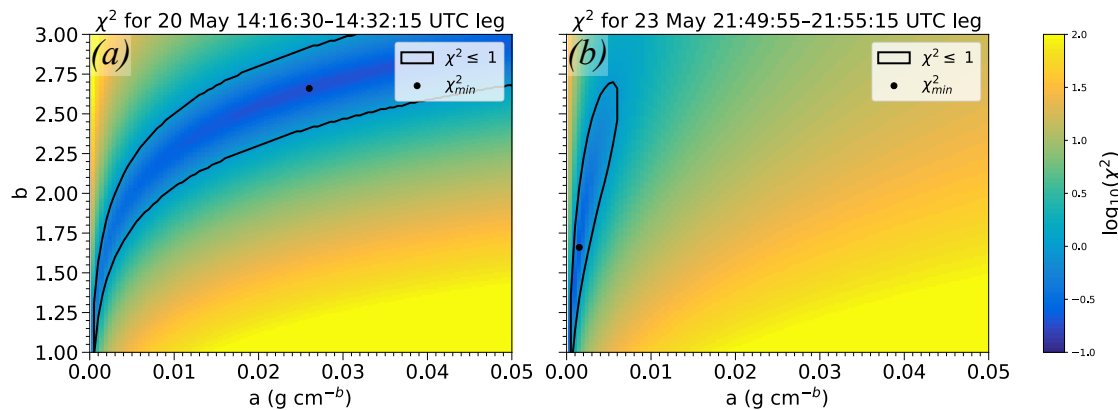
**Figure 15.** Same as in Fig. 12, but for (a) 14:16:30–14:32:15 UTC on 20 May and (b) 21:49:55–21:55:15 UTC on 23 May 2011. Outlined regions represent $\chi^2 \leq 1$ and the dots $\chi^2_{min}$.

**Table 1.** List of constant temperature flight legs used in the analysis for which coincident data between the ground-based radar and UND Citation exist. Start and end times, mean altitude, and temperature displayed.

| Mean Temp. [°C] | Mean Alt. [km] | Start Time [UTC] | End Time [UTC] |
|---|---|---|---|
| | | 25 April 2011 | |
| -22.0 | 6.8 | 11:42:50 | 11:49:00 |
| -26.5 | 7.4 | 11:05:20 | 11:14:45 |
| -26.5 | 7.4 | 11:21:20 | 11:34:05 |
| -35.5 | 8.3 | 10:03:05 | 10:08:45 |
| -35.5 | 8.3 | 10:11:10 | 10:20:15 |
| -35.5 | 8.3 | 10:28:30 | 10:35:45 |
| -35.5 | 8.3 | 10:51:15 | 10:59:10 |
| | | 20 May 2011 | |
| -5.5 | 5.0 | 13:41:25 | 13:52:00 |
| -10.5 | 5.9 | 13:54:05 | 14:00:05 |
| -16.0 | 6.9 | 14:35:30 | 14:40:35 |
| -23.0 | 7.9 | 14:16:30 | 14:32:15 |
| | | 23 May 2011 | |
| -25.0 | 7.9 | 21:49:55 | 21:55:15 |
| -25.0 | 7.9 | 22:06:45 | 22:11:00 |
| -34.5 | 9.1 | 22:32:50 | 22:37:15 |
| -34.5 | 9.1 | 22:41:35 | 22:48:20 |
| -34.5 | 9.1 | 22:58:40 | 23:03:40 |